SIAM J. Applied Dynamical Systems
Vol. 10, No. 2, pp. 469–509

© 2011 Society for Industrial and Applied Mathematics

# Shear-Induced Bifurcations and Chaos in Models of Three Coupled Lasers[*]

Nicholas Blackbeard[†], Hartmut Erzgräber[†], and Sebastian Wieczorek[†]

**Abstract.** We study nonlinear dynamics in a linear array of three coupled laser oscillators with rotational $\mathbb{S}^1$ and reflectional $\mathbb{Z}_2$ symmetry. The focus is on a *coupled-laser model* with dependence on three parameters: laser coupling strength, $\kappa$, laser frequency detuning, $\Delta$, and degree of coupling between the amplitude and phase of the laser, $\alpha$, also known as shear or nonisochronicity. Numerical bifurcation analysis is used in conjunction with Lyapunov exponent calculations to study the different aspects of the system dynamics. First, the shape and extent of regions with stable phase locking in the $(\kappa, \Delta)$ plane change drastically with $\alpha$. We explain these changes in terms of codimension-two and -three bifurcations of (relative) equilibria. Furthermore, we identify locking-unlocking transitions due to global homoclinic and heteroclinic bifurcations and the associated infinite cascades of local bifurcations. Second, vast regions of deterministic chaos emerge in the $(\kappa, \Delta)$ plane for nonzero $\alpha$. We give an intuitive explanation of this effect in terms of $\alpha$-induced stretch-and-fold action that creates horseshoes and discuss chaotic attractors with different topologies. Similar analysis of a more accurate *composite-cavity mode model* reveals good agreement with the *coupled-laser model* on the level of local and global bifurcations as well as chaotic dynamics, provided that coupling between lasers is not too strong. The results give new insight into modeling approaches and methodologies for studying nonlinear behavior of laser arrays.

**Key words.** coupled lasers, bifurcation analysis, Lyapunov exponents, codimension three, Belyakov bifurcation, $\mathbb{Z}_2$ symmetry

**AMS subject classifications.** 78A60, 34C15, 37G99

**DOI.** 10.1137/100817383

## 1. Introduction.

Lasers are nonlinear oscillators of great importance in modern technology (optical data storage and communication systems, laser sensors and radars, and large-scale displays), medicine (light therapy and surgery), and fundamental science (spectroscopy and interferometry). In particular, (semiconductor) *laser arrays* are intensively studied from two different viewpoints. From the applications viewpoint, owing to the recent technological progress, coupled lasers emerge as very compact sources of high-power radiation and are strongly desired in many of the applications mentioned above [9]. From the theoretical viewpoint, owing to their dynamical complexity, coupled lasers contribute to the field of dynamical systems with unexplored bifurcation structures and interesting nonlinear phenomena such as excitability [77, 61, 40, 83], various synchronization types [43, 67, 72, 57, 80], and spatial patterns [1, 52, 58]. Most importantly, laser systems provide a unique platform for experimental testing and exploiting these phenomena in real life applications such as chaos-based secure communication [3], ultrafast random-number generation [74], and instability-based radars and

---

[*] Received by the editors December 7, 2010; accepted for publication (in revised form) by J. Sieber March 9, 2011; published electronically June 7, 2011.

http://www.siam.org/journals/siads/10-2/81738.html

[†] College of Engineering, Mathematics, and Physical Sciences, University of Exeter, Exeter, UK EX4 4QF (n.blackbeard@exeter.ac.uk, h.erzgraber@exeter.ac.uk, s.m.wieczorek@exeter.ac.uk).

Copyright © by SIAM. Unauthorized reproduction of this article is prohibited.

sensors [45, 18]. This paper is concerned with modeling and numerical analysis of instabilities in (semiconductor) laser arrays.

There have been numerous theoretical and experimental studies concerning the nonlinear dynamics of coupled lasers. These studies have considered arrays of various sizes [10, 73, 58, 24], geometries [43, 67, 58], and different coupling types, including nearest-neighbor [85, 54, 43, 10, 73, 58, 24], global [60, 43, 39], and time-delayed coupling [32, 39, 86]. Many theoretical studies focused on simple ordinary differential equation (ODE) models [70, 54, 62, 43, 85, 10, 73, 58, 24], bifurcations in two-laser systems [70, 16, 62, 73, 36, 79, 81], and stability of synchronous solutions in larger arrays [10, 51, 58] with circular geometry (periodic boundary conditions) [54, 67, 44]. Some effort has been devoted to the analysis of more accurate composite-cavity mode models [64, 81] and partial differential equation (PDE) models [34, 1, 19, 37, 66, 78], including the Maxwell–Bloch equations [53]. Despite extensive and important previous work on the subject, there are still many unexplored problems concerning nonlinear behavior in laser arrays. Here, we focus on two such problems.

The first problem involves the stability and bifurcations of three nearest-neighbor coupled lasers in a linear array geometry found in commercially available laser arrays with dependence on three parameters: the coupling strength, $\kappa$, the frequency detuning, $\Delta$, and the linewidth enhancement factor, $\alpha$, that quantifies the degree of coupling between the amplitude and phase of an individual laser oscillator. On the one hand, by varying $\kappa$ and $\Delta$, we study laser-coupling conditions required to achieve stable phase locking, coupling-induced instabilities, and chaos. On the other hand, by varying $\alpha$, we uncover drastic differences in the ability of different laser types to phase lock or produce chaos. Specifically, our analysis explains the strong dependence of the three-laser phase locking characteristics on $\alpha$ reported in [24]. More generally, it contributes to the problem of nonlinear dynamics in coupled oscillators with shear (nonisochronicity) that cannot be captured by phase oscillator models alone [5, 46]. To explore the nonlinear dynamics of the coupled laser system in full extent, we perform three types of calculations. Lyapunov exponent calculations [55] identify regions with different attractors, including equilibria (phase locking), periodic or quasi-periodic oscillations, and chaos. Numerical bifurcation continuation [21] reveals the key qualitative changes in the system dynamics and identifies different locking-unlocking transitions due to local and global bifurcations. The results are presented as Lyapunov and bifurcation diagrams in the $(\kappa, \Delta)$ plane for different but fixed values of $\alpha$. Additionally, calculations demonstrating $\alpha$-induced phase space stretching and folding provide new insight into the complicated dynamical behavior observed for nonzero $\alpha$. The three-laser system considered here has the underlying topology and symmetry properties that are also found in larger linear laser arrays. Hence, its analysis is an important step in understanding the nonlinear behavior of larger arrays.

The second problem concerns different modeling approaches to studying instabilities in laser arrays. On the one hand, the partial differential Maxwell–Bloch equations give a very accurate physical description of strong optical nonlinearities imparted in coupled laser systems [62, 34, 1]. However, they are not well suited for stability and bifurcation analysis, which can provide insight into the mechanisms underlying synchronization, multistability, or coupling-induced instabilities. On the other hand, a simple coupled-laser model neglects certain spatial effects in optical coupling between lasers but is well suited for the stability and bifurcation analysis of even very large arrays [59, 58]. The coupled-laser model has been

Copyright © by SIAM. Unauthorized reproduction of this article is prohibited.

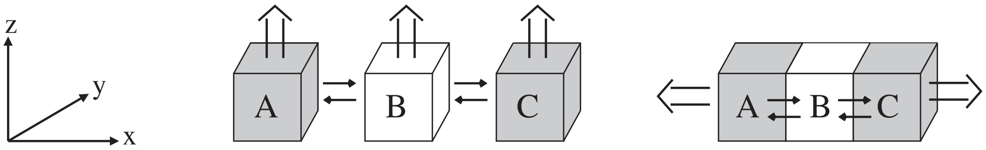

(a) Side–to–side (b) Face–to–face

**Figure 1.** *A sketch showing a linear array of three lasers coupled* (a) *side to side and* (b) *face to face. Small arrows indicate the direction of the coupling, and large arrows indicate the direction in which the laser beam propagates.*

shown to work well for just two coupled lasers [23], but it is not clear whether it accurately captures all the essential nonlinearities of larger arrays. To further verify its validity and understand its limitations, we compare results of the coupled-laser model with the more accurate composite-cavity mode model for the three-laser system.

This paper is organized as follows. In section 2 we discuss the system in physical terms and describe different realizations of the nearest-neighbor coupling between the lasers. In section 3 we describe two different modeling approaches leading to the composite-cavity mode model and the coupled-laser model. Then, in section 4, we carry out a detailed stability analysis of the coupled-laser model stressing the effect of $\mathbb{Z}_2$ symmetry on phase-locked solutions, the dependence of the locking regions on $\alpha$, locking-unlocking transitions associated with global bifurcations, and chaos owing to $\alpha$-induced stretching and folding of the phase space. Finally, section 5 contains a comparison between the simple coupled-laser model and the more accurate composite-cavity mode model.

## 2. System.

We consider a linear array of three lasers, denoted with a subscript $s = A, B, C$, that are coupled via their optical fields to their nearest neighbor(s) (Figure 1). A single laser is a nonlinear oscillator that consist of a "leaky" optical resonator and an active medium [17]. The optical resonator imposes resonant light oscillations, such as standing waves, that are called *optical modes*. The active medium consists of excited atoms, molecules, or electron-hole pairs that can amplify incident light and are referred to as *population inversion*. An optical mode can exhibit sustained oscillation if its frequency falls within the amplification band of the active medium and its amplification exceeds the losses. Otherwise, the mode decays exponentially to zero. Here, we assume that each laser is a single-mode laser, meaning that it operates with a single optical mode of natural frequency $\Omega_s$. Furthermore, all three lasers are identical apart from a possible natural-frequency detuning between the middle laser and the (resonant) outer lasers.

Two different physical realizations of optical coupling in a linear laser array are sketched in Figure 1, where the (resonant) outer lasers are shaded in grey. Small arrows indicate the direction of coupling, and large arrows indicate the direction in which the laser beam propagates. For *side-to-side* coupled lasers (Figure 1(a)), the coupling is due to the evanescent electric field transverse to the direction of the laser beam. Such a coupling realization has been studied, for example, in [38, 16, 85, 54, 1, 26, 43, 62, 67, 44, 10, 52, 73, 72, 57, 56, 58, 23, 48, 24]. For *face-to-face* coupled lasers (Figure 1(b)), the coupling is due to the electric field in the propagation direction of the laser beam. Such a coupling realization has been studied, for example, in [70, 27, 15, 50, 87, 81, 25].

Copyright © by SIAM. Unauthorized reproduction of this article is prohibited.

## 3. Different modeling approaches.

The spatiotemporal dynamics of the real-valued electric laser field $\mathcal{E}(\mathbf{r},t)$ is governed by the Maxwell equations and can be written as an inhomogeneous electromagnetic wave equation [63]:

$$-\nabla^2\mathcal{E}(\mathbf{r},t)+\mu_0\sigma\frac{\partial\mathcal{E}(\mathbf{r},t)}{\partial t}+\frac{n^2(\mathbf{r})}{c^2}\frac{\partial^2\mathcal{E}(\mathbf{r},t)}{\partial^2 t}=-\mu_0\frac{\partial^2\mathcal{P}(\mathbf{r},t)}{\partial t^2}. \tag{3.1}$$

The left-hand side of this PDE describes electric field propagation and losses within the laser array, whose physical structure is specified by the space-dependent refractive index, $n(\mathbf{r})$, and boundary conditions. The inhomogeneous term on the right-hand side involves the active-medium polarization, $\mathcal{P}(\mathbf{r},t)$, and represents the source of the propagating electric field. To calculate polarization and population inversion within each laser, (3.1) has to be combined with a suitable quantum-mechanical description of the active medium [63]. The resulting PDE model is known as the Maxwell–Bloch equations [31, 49].

In semiclassical laser theory [63], the inhomogeneous wave equation (3.1) is solved by expanding the electric field

$$\mathcal{E}(\mathbf{r},t)=\frac{1}{2}\sum_j U_j(\mathbf{r})A_j(t)+\overline{U}_j(\mathbf{r})\overline{A}_j(t) \tag{3.2}$$

(where the bar denotes complex conjugation) and the active-medium polarization

$$\mathcal{P}(\mathbf{r},t)=\frac{1}{2}\sum_j U_j(\mathbf{r})B_j(t)+\overline{U}_j(\mathbf{r})\overline{B}_j(t), \tag{3.3}$$

in terms of real-valued *optical modes*, $U_j(\mathbf{r})$, that are solutions to the homogeneous wave equation

$$-\nabla^2\mathcal{E}(\mathbf{r},t)+\frac{n^2(\mathbf{r})}{c^2}\frac{\partial^2\mathcal{E}(\mathbf{r},t)}{\partial^2 t}=0. \tag{3.4}$$

Here, we assume *passive optical modes* $U_j(\mathbf{r})$ that do not depend on the instantaneous population inversion. This assumption is justified when population-induced contributions to the refractive index, or their variations, remain negligible. However, when those contributions vary enough to change the mode profiles, one needs to consider *active optical modes* that do depend on the instantaneous population inversion [78, 66]. Substituting a field of a passive eigenmode with a frequency $\Omega_j$,

$$\mathcal{E}(\mathbf{r},t)=U_j(\mathbf{r})\,e^{-i\Omega_j t},$$

into (3.4) gives the Helmholtz equation for $U_j(\mathbf{r})$:

$$\nabla^2 U_j(\mathbf{r})+\frac{n^2(\mathbf{r})}{c^2}\,\Omega_j^2\,U_j(\mathbf{r})=0. \tag{3.5}$$

For suitably chosen boundary conditions, passive optical modes are orthogonal with a weight function $n^2(\mathbf{r})$, meaning that they satisfy the orthogonality relation

$$\int_{\mathbb{R}^3} n^2(\mathbf{r})\,U_j(\mathbf{r})\,U_{j'}(\mathbf{r})\,d\mathbf{r}=\mathcal{N}\,\delta_{j\,j'}, \tag{3.6}$$

Copyright © by SIAM. Unauthorized reproduction of this article is prohibited.

with an arbitrary normalization constant, $\mathcal{N}$, and the Kronecker delta, $\delta_{j\,j'}$. The time-dependent and complex-valued coefficients of the field expansion (3.2), $A_j(t)$, are the corresponding electric field amplitudes. Given the passive optical modes $U_j(\mathbf{r})$, equations for $A_j(t)$ are obtained by substituting expansions (3.2)–(3.3) into (3.1) and projecting onto $U_j(\mathbf{r})$ [63]. It is common to separate in $A_j(t)$ a term oscillating at a fast optical frequency, $\nu$, by writing

$$A_j(t) = E_j(t)\, e^{-i\nu t} \tag{3.7}$$

and to study the slowly varying, complex-valued field amplitude, $E_j(t)$. This is accomplished through a number of approximations described in [63, 17], including the *rotating wave approximation* that removes the complex-conjugated terms in (3.2)–(3.3) and introduces the rotational symmetry discussed in section 4.1.

Our paper considers two different approaches to modeling laser arrays within the framework of semiclassical laser theory: the *coupled-laser approach* in section 4 and the *composite-cavity mode approach* in section 5. These approaches arise from different ways of calculating the passive optical modes $U_j(\mathbf{r})$ or, in other words, from the different eigenbasis used in expansions (3.2)–(3.3).

## 4. Coupled-laser approach.

In the coupled-laser approach, laser coupling is completely neglected in solving the homogeneous wave equation (3.4), which is justified for weakly coupled lasers. The solutions $U_j(\mathbf{r})$ are then simply the passive optical modes of the individual uncoupled lasers with constant refractive index $n$. The coupling is accounted for by an additional source term in the right-hand side of the inhomogeneous wave equation for each individual laser [69, 70, 62, 23]. The resulting set of ODEs can be thought of as a space-discretized version of the original Maxwell–Bloch equations with adiabatically eliminated polarization (class-B lasers [83]). Specifically, the three-laser system sketched in Figure 1 can be modeled by rate equations for the normalized slowly varying complex-valued electric fields, $E_s$,

$$\begin{aligned}\frac{dE_A}{dt} &= \beta\gamma(1-i\alpha)N_A E_A - i(\Omega_A-\nu)E_A + i\kappa E_B,\\ \frac{dE_B}{dt} &= \beta\gamma(1-i\alpha)N_B E_B - i(\Omega_B-\nu)E_B + i\kappa(E_A+E_C),\\ \frac{dE_C}{dt} &= \beta\gamma(1-i\alpha)N_C E_C - i(\Omega_C-\nu)E_C + i\kappa E_B,\end{aligned} \tag{4.1}$$

and the normalized real-valued population inversions, $N_s$,

$$\frac{dN_s}{dt} = \Lambda - (N_s+1) - (1+\beta N_s)|E_s|^2 \quad \text{for} \quad s = A, B, C, \tag{4.2}$$

where $t$ is the normalized time. Different derivations of (4.1)–(4.2) from (3.1) are found in [69, 70, 62, 23].

The optical coupling between lasers is described by the last terms of equations (4.1), where $\kappa$ is the normalized coupling strength. The coupled-laser model (4.1)–(4.2) can describe both physical realizations of optical coupling from Figure 1, provided that the coupling is weak

Copyright © by SIAM. Unauthorized reproduction of this article is prohibited.

enough and that there are no gaps between the face-to-face coupled lasers (Figure 1(b)).[1] For the different realizations, the coupling strength, $\kappa$, depends on different physical parameters. For side-to-side coupling (Figure 1(a)), $\kappa$ is a function of the distance, $d$, between the lasers [72, 62, 23]:

$$\kappa \sim e^{-d}.$$

For face-to-face coupling (Figure 1(b)), $\kappa$ is a function of the transmission coefficient, $T$, of the common coupling mirror between the lasers and the length, $L$, of the optical resonator [70]:

$$\kappa \sim \frac{\sqrt{T}}{L\sqrt{1-T}}.$$

The weak-coupling assumption implies a sufficiently large distance, $d$, or a sufficiently low transmission coefficient, $T$, of the coupling mirror separating the lasers. Given that the outer lasers have the same natural frequency, $\Omega_A = \Omega_C = \Omega_{A,C}$, we set the reference frequency, $\nu$, to be

$$\nu = \Omega_B$$

and define the normalized frequency detuning between the middle and two outer lasers:

$$\Delta = \Omega_B - \Omega_{A,C}. \tag{4.3}$$

The symmetry-breaking effects of different outer lasers have been studied in [24].

An important property of a single laser oscillator is the coupling between the amplitude and the phase of the complex-valued laser field, $E_s(t)$. Its physical origin is the dependence of the refractive index of the active medium—and hence the laser resonant frequency—on the population inversion [33]. This property is quantified by the linewidth enhancement factor, $\alpha$, henceforth called the $\alpha$-parameter. It takes values between 0 and 1 for gas and solid state lasers, and between 1 and 10 for typical semiconductor lasers. While $\alpha$ does not influence the stability of a single laser, it introduces a special property in the phase space. For $\alpha = 0$, trajectories with different $|E_s|$ rotate with the same frequency about the origin. However, if $\alpha > 0$, trajectories with larger $|E_s|$ rotate faster, giving rise to $\alpha$-dependent phase space stretching along the angular direction in the complex $E_s$ plane. The resulting *stretch-and-fold action* is important for the discussion of coupling-induced chaos in section 4.6. More generally, amplitude-phase coupling is a universal property of nonlinear oscillators and appears in various scientific disciplines under different names. In dynamical systems and biology, one speaks of shear, twist, or nonisochronicity [5, 46], in physics of nonlinear dispersion [77], and in engineering of self-phase modulation or chirp [33].

---

[1] If there are gaps between face-to-face coupled lasers, one needs to include additional equations for the field dynamics within the gap (gap size comparable to the laser size) or time delay in the coupling terms satisfying appropriate boundary conditions (gap size larger than the laser size).

Copyright © by SIAM. Unauthorized reproduction of this article is prohibited.

**Table 1**

*The laser parameters and their values* [81].

| Parameter | Description | Value |
|---|---|---|
| $\gamma$ | ratio of field and population decay rates | 100 |
| $\beta$ | normalized gain coefficient | 5.16 |
| $\Lambda$ | normalized pump rate | 3 |
| $\kappa$ | normalized coupling strength | $[0, 50]$ |
| $\Delta = \Omega_B - \Omega_{A,C}$ | normalized frequency detuning | $[-60, 60]$ |
| $\alpha$ | linewidth enhancement factor | $[0, 2]$ |

The remaining parameters are the normalized gain coefficient, $\beta$, the ratio of the field and population inversion decay rates, $\gamma$, and the normalized pump rate, $\Lambda$. The parameter values used here are given in Table 1.

### 4.1. Symmetry properties.

Knowledge of the symmetries present in a system of ODEs can be used to facilitate their analysis. The coupled-laser model (4.1)–(4.2) has $\mathbb{S}^1 \times \mathbb{Z}_2$ symmetry [28]. Here, we reduce the $\mathbb{S}^1$ symmetry to facilitate the bifurcation analysis and make use of $\mathbb{Z}_2$ symmetry to distinguish between solution types with different sets of generic bifurcations.

The (continuous) $\mathbb{S}^1$ symmetry is due to the equivariance of the vector field defined by (4.1)–(4.2) under the transformation

$$\begin{aligned} T_{\mathbb{S}^1} :& (E_A, E_B, E_C, N_A, N_B, N_C)^T \\ & \longrightarrow (e^{ia}E_A, e^{ia}E_B, e^{ia}E_C, N_A, N_B, N_C)^T \quad \forall a \in [0, 2\pi). \end{aligned} \tag{4.4}$$

This transformation corresponds to the same phase shift in all the laser fields, $E_s$, and can be represented by the matrix

$$R_{\mathbb{S}^1} = \begin{pmatrix} I_3\, e^{ia} & 0 \\ 0 & I_3 \end{pmatrix}, \tag{4.5}$$

where $I_3$ is the $3 \times 3$ identity matrix. As a result, the simplest nonzero solution of (4.1)–(4.2) is an $\mathbb{S}^1$ group orbit or a *relative equilibrium* in the form of a limit cycle or a circle of nonhyperbolic equilibria. A group orbit reduction [13] greatly facilitates numerical bifurcation analysis, as it allows, for example, periodic $\mathbb{S}^1$ group orbits to be studied as isolated equilibria in the group orbit space. To carry out the group orbit reduction, we express the complex-valued electric fields, $E_s(t)$, in terms of their amplitudes, $|E_s(t)|$, and phases, $\varphi_s(t)$:

$$E_s(t) = |E_s(t)|e^{i\varphi_s(t)}. \tag{4.6}$$

Substituting (4.6) into the electric field equations (4.1), introducing the phase differences,

$$\varphi_{BA} = \varphi_B - \varphi_A, \qquad \varphi_{BC} = \varphi_B - \varphi_C, \tag{4.7}$$

Copyright © by SIAM. Unauthorized reproduction of this article is prohibited.

and using (4.3) gives

$$\begin{aligned}
\frac{d|E_A|}{dt} &= \beta\gamma N_A|E_A| - \kappa|E_B|\sin\varphi_{BA},\\
\frac{d|E_B|}{dt} &= \beta\gamma N_B|E_B| + \kappa|E_A|\sin\varphi_{BA} + \kappa|E_C|\sin\varphi_{BC},\\
\frac{d|E_C|}{dt} &= \beta\gamma N_C|E_C| - \kappa|E_B|\sin\phi_{BC},\\
\frac{d\varphi_{BA}}{dt} &= \kappa\left(\frac{|E_A|}{|E_B|} - \frac{|E_B|}{|E_A|}\right)\cos\varphi_{BA} + \kappa\frac{|E_C|}{|E_B|}\cos\varphi_{BC}\\
&\quad - \alpha\beta\gamma(N_B - N_A) - \Delta,\\
\frac{d\varphi_{BC}}{dt} &= \kappa\left(\frac{|E_C|}{|E_B|} - \frac{|E_B|}{|E_C|}\right)\cos\varphi_{BC} + \kappa\frac{|E_A|}{|E_B|}\cos\varphi_{BA}\\
&\quad - \alpha\beta\gamma(N_B - N_C) - \Delta.
\end{aligned}\tag{4.8}$$

The electric field equations (4.8) along with the population inversion equations (4.2) give an eight-dimensional *reduced system* without $\mathbb{S}^1$ symmetry. Clearly, a regular equilibrium for the reduced system corresponds to a limit cycle ($d\varphi_s/dt \neq 0$ for $s = A, B, C$) or a circle of nonhyperbolic equilibria ($d\varphi_s/dt = 0$ for $s = A, B, C$) for the original system (4.1)–(4.2). One drawback of this approach is that it introduces singularities in the phase difference equations when $|E_s| = 0$. Since a laser field is typically nonzero above the lasing threshold ($\Lambda > 1$), the reduced system (4.2) and (4.8) works well in practice.

The (discrete) $\mathbb{Z}_2$ symmetry is due to the equivariance of the vector field defined by (4.2) and (4.8) under the linear transformation

$$\begin{aligned}
T_{\mathbb{Z}_2} :&(|E_A|, |E_B|, |E_C|, \varphi_{BA}, \varphi_{BC}, N_A, N_B, N_C)^T\\
&\longrightarrow (|E_C|, |E_B|, |E_A|, \varphi_{BC}, \varphi_{BA}, N_C, N_B, N_A)^T.
\end{aligned}\tag{4.9}$$

In physical terms, $T_{\mathbb{Z}_2}$ corresponds to swapping the outer two lasers and can be represented by the matrix

$$R_{\mathbb{Z}_2} = \begin{pmatrix} A_3 & 0 & 0\\ 0 & A_2 & 0\\ 0 & 0 & A_3 \end{pmatrix},\tag{4.10}$$

where $A_n$ is an $n \times n$ antidiagonal identity matrix. $R_{\mathbb{Z}_2}$ along with the identity matrix $I_8$ forms a representation of the group $\mathbb{Z}_2$. The *fixed-point subspace* [28] due to the $\mathbb{Z}_2$ symmetry,

$$\begin{aligned}
\mathrm{Fix}(\mathbb{Z}_2) = \{&(|E_A|, |E_B|, |E_C|, \varphi_{BA}, \varphi_{BC}, N_A, N_B, N_C)^T \in \mathbb{R}^8 :\\
&|E_A| = |E_C|,\quad \varphi_{BA} = \varphi_{BC},\quad N_A = N_C\},
\end{aligned}\tag{4.11}$$

is a five-dimensional manifold that is invariant under the transformation (4.9) and under the flow given by (4.2) and (4.8). We are interested in compact sets that are invariant under the

Copyright © by SIAM. Unauthorized reproduction of this article is prohibited.

flow given by (4.2) and (4.8) (e.g., equilibrium points, limit cycles, tori) and refer to them as *closed invariant sets.*

A trajectory in the fixed-point subspace, $X_1(t) \in \mathrm{Fix}(\mathbb{Z}_2)$, satisfies

$$R_{\mathbb{Z}_2} X_1(t) = X_1(t) \;\text{ for all } t \in \mathbb{R} \tag{4.12}$$

and is called a *fixed trajectory.* Fixed trajectories correspond to a situation where the outer lasers are synchronized in phase, meaning that they have the same field amplitude, phase, and population inversion. Clearly, a closed invariant set, $X_1 \in \mathrm{Fix}(\mathbb{Z}_2)$, is $R_{\mathbb{Z}_2}$-invariant,

$$R_{\mathbb{Z}_2} X_1 = X_1, \tag{4.13}$$

and we call it a *fixed closed invariant set.* A trajectory not in the fixed-point subspace, $X_1(t) \notin \mathrm{Fix}(\mathbb{Z}_2)$, satisfies

$$R_{\mathbb{Z}_2} X_1(t) = X_2(t) \neq X_1(t) \;\text{ for any } t \in \mathbb{R}, \tag{4.14}$$

and we call it a *conjugate trajectory.* Conjugate trajectories correspond to the situation where the outer lasers have different field amplitudes, phases, and inversions. However, there are two types of closed invariant sets that are not fixed. The first type is a closed invariant set, $X_1 \notin \mathrm{Fix}(\mathbb{Z}_2)$, that is not $R_{\mathbb{Z}_2}$-invariant and satisfies

$$R_{\mathbb{Z}_2} X_1 = X_2 \neq X_1, \tag{4.15}$$

where $X_1$ and $X_2$ are *conjugate closed invariant sets.* The second type is a closed invariant set, $X_1 \notin \mathrm{Fix}(\mathbb{Z}_2)$, that is $R_{\mathbb{Z}_2}$-invariant because it satisfies (4.13) rather than (4.15). We call such a set *a symmetric closed invariant set.* This classification is important in bifurcation theory, as the $\mathbb{Z}_2$ symmetry places restrictions on the Jacobian of the system that lead to different generic bifurcations for fixed, conjugate, and symmetric closed invariant sets [28]. Bifurcations of conjugate closed invariant sets happen as in systems without symmetry. Also, a bifurcation of $X_1$ implies the same bifurcation of the symmetric counterpart $X_2$. In the two-parameter diagrams, we use a star (*) to indicate double bifurcations of conjugate equilibria and conjugate limit cycles. However, bifurcations of symmetric and fixed invariant sets are different. For example a pitchfork bifurcation is generic in system (4.2) and (4.8) but only for fixed equilibria as well as fixed and symmetric limit cycles. Also, symmetric limit cycles cannot have the simple Floquet multiplier of $-1$ and period double (this is true for $\mathbb{Z}_k$ symmetry with even $k$), while fixed and conjugate limit cycles can [42, Chap. 7.4]. Note that a symmetric limit cycle corresponds to the situation where the two outer lasers exchange their role after half a period [42, Chap. 7.4].

Finally, there is the parameter symmetry

$$(\varphi_{BA}, \varphi_{BC}, \alpha, \Delta) \longrightarrow (-\varphi_{BA} + \pi, -\varphi_{BC} + \pi, -\alpha, -\Delta). \tag{4.16}$$

It implies that if $\alpha = 0$, the bifurcation diagram in the $(\kappa, \Delta)$ plane has reflectional symmetry about the line $\Delta = 0$.

Copyright © by SIAM. Unauthorized reproduction of this article is prohibited.

**4.2. Phase locking.** We are interested in the stability of *phase-locked* solutions

$$\begin{aligned} E_s(t) &= |E_s^0| e^{-i(\omega^0 t + \varphi_s^0)}, \\ N_s(t) &= N_s^0 \quad \text{for } s = A, B, C, \end{aligned} \tag{4.17}$$

where all three lasers synchronize to the same optical frequency $\omega^0$ and have constant nonzero amplitudes $|E_s^0|$, constant phase shifts $\varphi_s^0$, and constant population inversions $N_s^0$. A phase-locked solution (4.17) with $\omega^0 \neq 0$ is a limit cycle for the original system (4.1)–(4.2) and an isolated equilibrium for the reduced system (4.2) and (4.8). In the Lyapunov and bifurcation diagrams, parameter regions with stable phase-locked solutions (4.17) are shaded in green.

**4.3. Overview of the dynamics in the coupled-laser model.** The two Lyapunov diagrams in Figure 2, for $\alpha = 0$ and $\alpha = 1$, give a rough overview of different attractor types and are used to motivate more detailed (bifurcation) analysis.[2]

For $\alpha = 0$, the $(\kappa, \Delta)$ plane is dominated by stable limit cycles, where the greyscale quantifies the convergence rate along the leading direction. Stable phase locking occurs in the two green bands around the lines $\kappa = \pm\Delta$, meaning that lasers can phase lock for any coupling strength, $\kappa$, provided that the frequency detuning, $\Delta$, is sufficiently large. In Figure 2(a) the green bands of phase locking are interrupted with grey intervals due to bistability. Interestingly, we find no stable tori nor chaotic attractors for $\alpha = 0$. Note that the Lyapunov diagram (Figure 2(a)) has reflectional symmetry about the line $\Delta = 0$ in agreement with (4.16). In contrast, for $\alpha = 1$, the $(\kappa, \Delta)$ plane is dominated by chaotic attractors, where the yellow-red scale quantifies the associated divergence rate. Furthermore, different regions with stable tori appear as indicated in blue. Stable phase locking is confined to a small parameter region around $\Delta = 0$ and small $\kappa$, meaning that above some critical coupling strength the lasers cannot phase lock for any $\Delta$. Stable limit cycles are found mainly for small $\kappa$. As expected from the symmetry (4.16), the diagram in Figure 2(b) does not have reflectional symmetry.

Clearly, there are a number of striking differences between Figures 2(a) and (b). First, there is a big difference in the shape and extent of the stable phase locking regions plotted in green. Second, we note the appearance of vast chaotic regions for nonzero $\alpha$. Third, different attractor types found in the vicinity of the phase locking regions suggest rather different mechanisms underlying the locking-unlocking transitions. In the following sections we address these three points in more detail by combining Lyapunov exponent calculations, numerical bifurcation continuation [21], and simulations demonstrating $\alpha$-induced phase space stretching and folding.

**4.4. Local bifurcations of phase-locked solutions.** The different types of equilibria of (4.2) and (4.8) correspond to different types of phase locking. A fixed equilibrium (4.13)

---

[2] To calculate Lyapunov exponents [7], we discretize the $(\kappa, \Delta)$ parameter plane into a grid of $800 \times 800$ points. For each fixed value of $\Delta$ we sweep the parameter $\kappa$ using the final point on the trajectory (slightly perturbed) as an initial condition for the subsequent value of $\kappa$. For calculations we use the original system (4.1)–(4.2) to avoid possible singularities at $E_s = 0$ in the vector field of the reduced system (4.2) and (4.8). Owing to the $\mathbb{S}^1$ symmetry of the original system, there is always one zero Lyapunov exponent that corresponds to the drift along the group orbit. The remaining Lyapunov exponents are used to distinguish between different attractors for the reduced system (4.2) and (4.8) as shown in Table 2.

Copyright © by SIAM. Unauthorized reproduction of this article is prohibited.

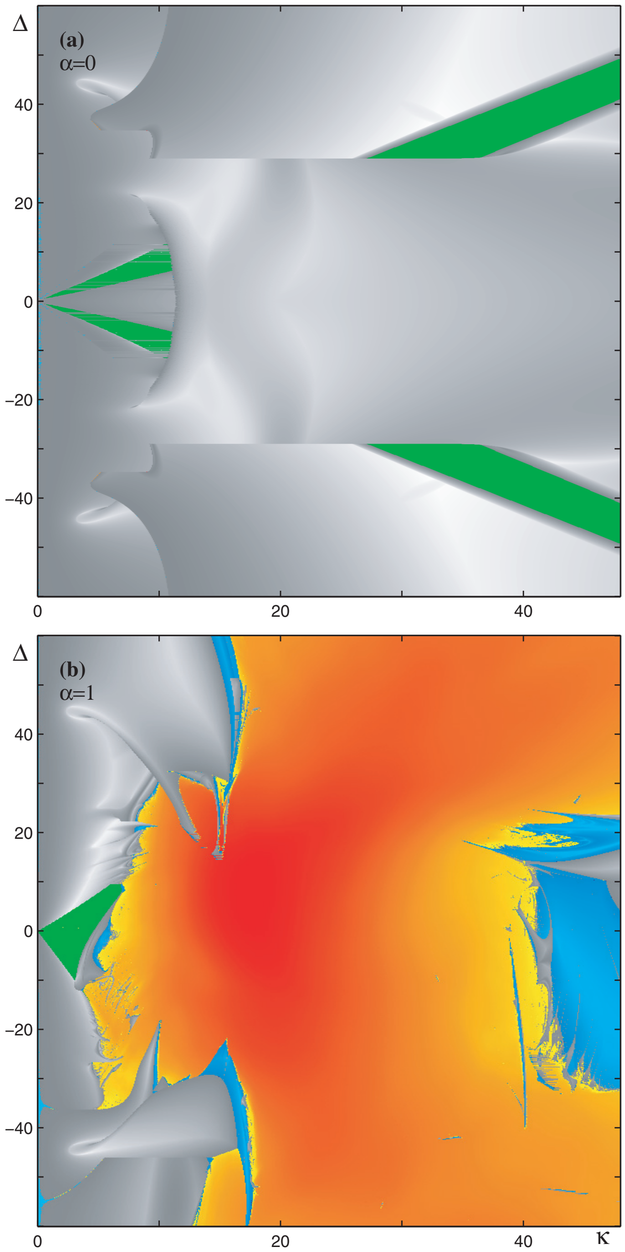

**Figure 2.** *Lyapunov diagrams for the reduced system* (4.2) *and* (4.8) *in the* $(\kappa, \Delta)$ *parameter plane for* (a) $\alpha = 0$ *and* (b) $\alpha = 1$*, obtained by decreasing* $\kappa$*. For the color coding see Table* 2.

satisfies

$$E_A = E_C \quad \text{and} \quad N_A = N_C \tag{4.18}$$

and describes a situation where the outer lasers oscillate in phase with each other and typically out of phase with the middle laser. *Fixed-locking regions* contain stable fixed equilibria and

Copyright © by SIAM. Unauthorized reproduction of this article is prohibited.

**Table 2**

*The color coding used in Lyapunov diagrams for classification of different types of attractors of the reduced system* (4.2) *and* (4.8).

| Key | Attractor type | Lyapunov exponents $\mu_i$ |
|---|---|---|
| 🟩 | equilibrium $\Rightarrow$ phase locking | $\mu_i < 0$ for $i = 1..8$ |
| ⬜ | limit cycle (weakly-strongly attracting) | $\mu_1 = 0, \mu_i < 0$ for $i = 2..8$ |
| 🟦 | torus (weakly-strongly attracting) | $\mu_1 = \mu_2 = 0, \mu_i < 0$ for $i = 3..8$ |
| 🟧 | chaotic attractor (slow-fast divergence) | at least one $\mu_i > 0$ |

are indicated by light green shading in the bifurcation diagrams. A conjugate equilibrium (4.15) satisfies

$$E_A \neq E_C \quad \text{and/or} \quad N_A \neq N_B \tag{4.19}$$

and describes out-of-phase locking between all three lasers. *Conjugate-locking regions* contain stable conjugate equilibria and are indicated by dark green shading in the bifurcation diagrams. Bifurcations of equilibria define boundaries of the locking regions. Given the $\mathbb{Z}_2$ symmetry of (4.2) and (4.8), the set of generic codimension-one bifurcations of equilibria includes saddle-node (S), pitchfork (P), and Hopf (H) bifurcations. These bifurcations are two-dimensional surfaces in the three-dimensional $(\kappa, \Delta, \alpha)$ parameter space and can be computed [21] as curves in the $(\kappa, \Delta)$ plane for different but fixed values of $\alpha$. Crossings or tangencies between different codimension-one bifurcations of the same equilibrium typically give rise to codimension-two bifurcations. They are curves in the $(\kappa, \Delta, \alpha)$ parameter space that indicate changes in the type of locking boundary. Codimension-two bifurcations include saddle-node-Hopf (SH), pitchfork-Hopf (PH), double-Hopf (HH), and Bogdanov–Takens (BT) bifurcations, and they are marked with black dots in the $(\kappa, \Delta)$ plane. In the $(\kappa, \Delta, \alpha)$ parameter space, different bifurcation curves of codimension two can merge at special points of codimension higher than two. Table 3 contains a summary of the bifurcation diagram coding.

**4.4.1. Bifurcations of codimensions one and two.** Bifurcation diagrams in the $(\kappa, \Delta)$ plane for different but fixed values of $\alpha \in [0, 1]$ are shown in Figures 3 and 4, where the thick curves indicate bifurcations of stable phase-locked solutions. For $\alpha = 0$ (Figure 3(a)), we restrict the discussion to the positive half plane owing to the parameter symmetry (4.16). Three different bifurcations of stable phase-locked solutions emerge from the origin such that stable locking is found within the green-shaded band around $\kappa = \Delta$. This is similar to the Lyapunov diagram in Figure 2(a). The upper boundary of the fixed-locking region (light green) starts at the origin as a saddle-node curve (S) representing bifurcations *within* the fixed-point subspace Fix($\mathbb{Z}_2$) and switches to a Hopf curve (H) via a saddle-node-Hopf (SH) bifurcation point. The lower boundary of the fixed-locking region starts at the origin as a pitchfork curve (P), undergoes a pitchfork-Hopf (PH) bifurcation, and also changes to a Hopf curve. Both Hopf curves extend to large $\kappa$ where they become parallel to each other, giving rise to an unbounded locked region. Hence, stable fixed locking is possible for any coupling strength, $\kappa$. In contrast, the conjugate-locking region (dark green) is entirely bounded by a pitchfork, a saddle-node, and two Hopf curves, meaning that stable conjugate-locking cannot be achieved above some critical value of $\kappa$. The supercritical part of the pitchfork curve,

Copyright © by SIAM. Unauthorized reproduction of this article is prohibited.

**Table 3**

*The labeling, color coding, and shading of the bifurcation diagrams.* $\lambda_s$ *and* $\lambda_u$ *are the stable and unstable eigenvalues of a saddle within the homoclinic/heteroclinic center manifold.*

| Symbol | Key | Bifurcation/Solution |
|---|---|---|
| S | 🟦 | saddle-node bifurcation |
| Shom | ⬛ | saddle-node homoclinic bifurcation |
| P | 🟧 | pitchfork bifurcation |
| H | 🟥 | Hopf bifurcation |
| SL | 🟦 | saddle-node of limit cycle bifurcation |
| PL | 🟪 | pitchfork of limit cycle bifurcation |
| PD | 🟩 | period-doubling bifurcation |
| T | ⬛ | torus (Neimark–Sacker) bifurcation |
| hom | ⬛ | homoclinic bifurcation |
| het | ⬛ | heteroclinic (relative homoclinic) bifurcation |
| SH | ● | saddle-node-Hopf bifurcation |
| PH | ● | pitchfork-Hopf bifurcation |
| HH | ● | double-Hopf bifurcation |
| PS | ● | pitchfork-saddle-node bifurcation |
| BT | ● | Bodganov–Takens bifurcation |
| PSL | ● | pitchfork-saddle-node of limit cycle bifurcation |
| PT | ● | pitchfork-torus bifurcation |
| $1:2$ | ● | 1:2 resonance |
| $\delta_{-1}$ | ● | homoclinic Belyakov bifurcation where $\frac{\Re(\lambda_s)}{\Re(\lambda_u)} = -1$ |
| $\delta_{-0.5}$ | ● | homoclinic Belyakov bifurcation where $\frac{\Re(\lambda_s)}{\Re(\lambda_u)} = -0.5$ |
| ShH | ● | relative Shilnikov–Hopf bifurcation |
| NC | ● | noncentral saddle-node homoclinic bifurcation |
|  | * | double bifurcations of conjugate equilibria and conjugate limit cycles that are not $R_{\mathbb{Z}_2}$-invariant |
|  | 🟩 | stable fixed equilibria/phase-locked solutions (4.18) |
|  | 🟩 | stable conjugate equilibria/phase-locked solutions (4.19) |

between the origin and PS*, forms the boundary between fixed and conjugate locking. At PS*, the upper boundary of the conjugate-locking region changes to a saddle-node curve, and the pitchfork bifurcation becomes subcritical. This gives rise to a small region of tristability between two conjugate equilibria and a fixed equilibrium.

For $\alpha = 0.1$ (Figure 3(b)) the symmetry of the bifurcation diagram is broken in agreement with (4.16). The left boundary of the upper ($\Delta > 0$) locking band is now given by a pitchfork-saddle-node point (PS*) that has emerged from the origin, giving rise to an open interval of small $\kappa$ where the lasers can phase lock only if $\Delta < 0$. The lower boundary of the upper conjugate-locking region involves an additional Hopf curve due to a codimension-three triple-Hopf bifurcation at $\alpha \approx 0.04$ that is discussed in more detail in section 4.4.2. The lower ($\Delta < 0$) locking region remains qualitatively unchanged at small $\kappa$ but becomes bounded at large $\kappa$ as the two Hopf curves forming its boundary intersect at a double-Hopf point at $(\kappa, \Delta) \approx (92, 91)$ (not shown in the figure).

As $\alpha$ is increased, the pitchfork-saddle-node point (PS) indicating the left boundary of the upper ($\Delta > 0$) locking region shifts further away from the origin and reaches $(\kappa, \Delta) \approx (14.9, 15.1)$ for $\alpha = 0.2$ (Figure 3(c)). Due to a codimension-three bifurcation involving a

Copyright © by SIAM. Unauthorized reproduction of this article is prohibited.

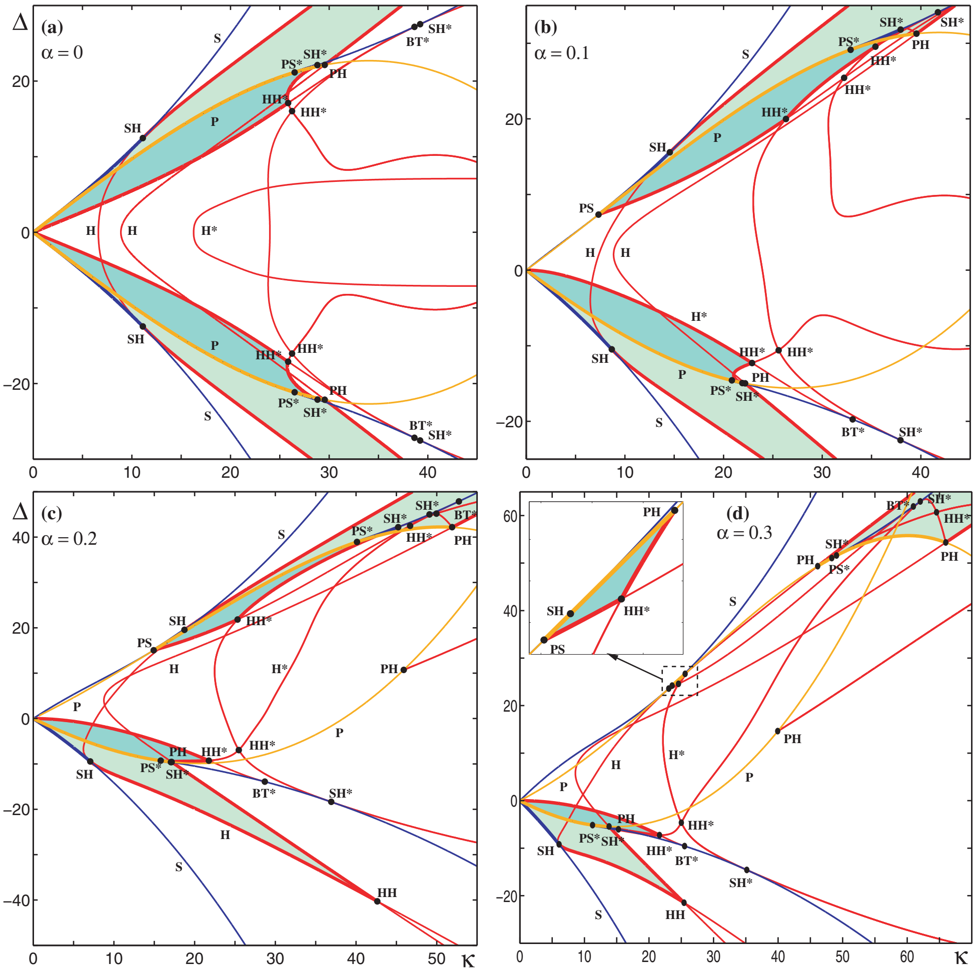

**Figure 3.** *Two-parameter bifurcation diagrams in the* $(\kappa, \Delta)$ *plane for different values of* $\alpha$*. Regions of locking are shaded in green. Light and dark shading correspond to different types of phase locking defined by* (4.18) *and* (4.19)*, respectively. Curves represent codimension-one bifurcations, and black dots indicate where crossings and tangencies between different bifurcation curves give rise to codimension-two bifurcation points. For the labeling, color coding, and shading see Table* 3.

double-Hopf (HH$^*$) and two saddle-node-Hopf (SH$^*$) points, there are changes to the boundary of the upper conjugate-locking region at larger $\kappa$. Namely, it consists of one less Hopf curve, one less double-Hopf point, and a different saddle-node-Hopf point. Concurrently, the double-Hopf point (HH) indicating the right boundary of the lower ($\Delta < 0$) locking region shifts towards the origin. As a result of these transitions, there is an increase in the interval of $\kappa$ where stable phase locking is impossible for $\Delta > 0$ and a decrease in the interval of $\kappa$ where stable phase locking is possible for $\Delta < 0$.

Between $\alpha = 0.2$ and $\alpha = 0.3$ the locking region for $\Delta > 0$ splits into two parts as the $(\kappa, \Delta)$ plane becomes tangent to a minimum of a codimension-two pitchfork-Hopf curve in the $(\kappa, \Delta, \alpha)$ parameter space. This bifurcation is discussed in more detail in section 4.4.2, but its effects can be seen for $\alpha = 0.3$ (Figure 3(d)). The striking new feature is an open

Copyright © by SIAM. Unauthorized reproduction of this article is prohibited.

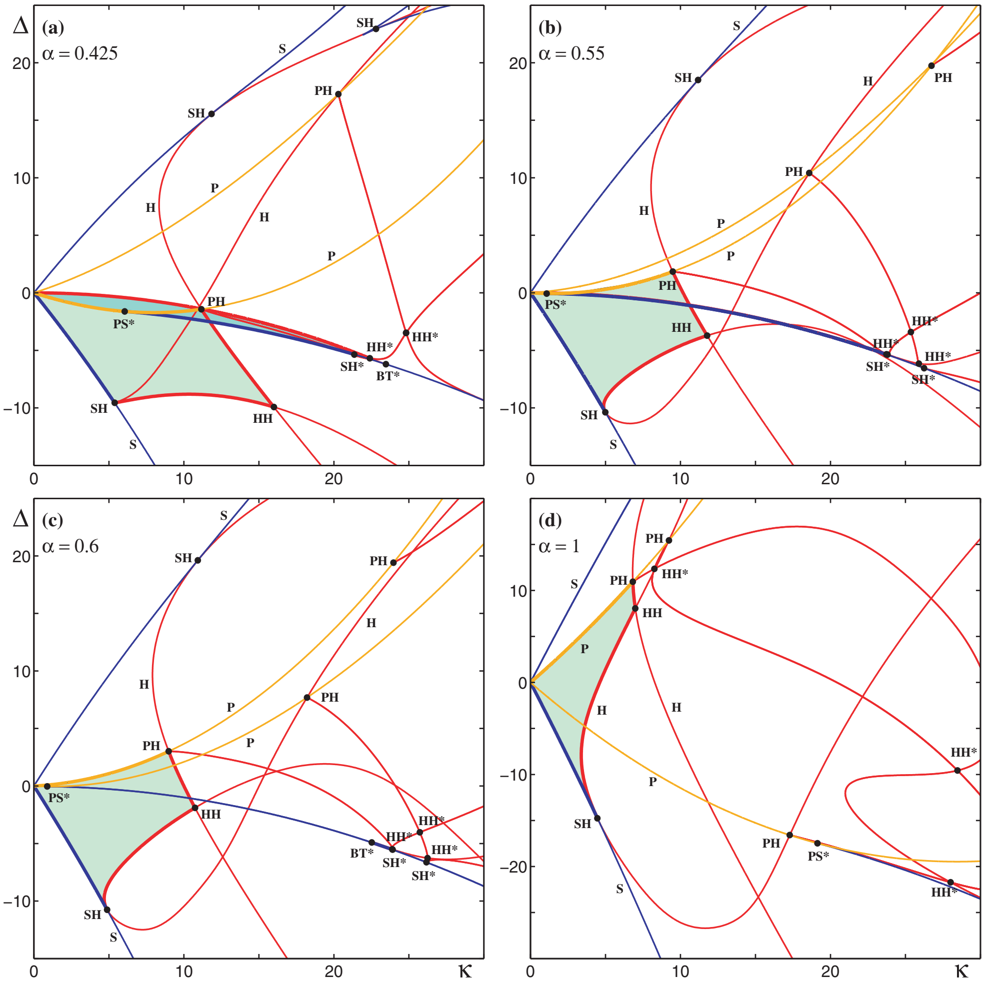

**Figure 4.** *Continuation of Figure 3 showing two-parameter bifurcation diagrams in the $(\kappa, \Delta)$ plane for different values of $\alpha$. Curves represent codimension-one bifurcations, and black dots indicate where crossings and tangencies between different bifurcation curves give rise to codimension-two bifurcation points. For the labeling, color coding, and shading see Table 3.*

interval of the coupling strength, at around $25.6 < \kappa < 46.1$, where stable phase locking is no longer possible for any value of the frequency detuning, $\Delta$. On the right-hand side of this interval, the locking region (dominated by fixed locking) is found only for $\Delta > 0$. It is bounded by a pitchfork and two Hopf curves at lower $\kappa$ but remains unbounded for increasing $\kappa$. On the left-hand side of this interval, there are two separate locking regions. The larger locking region for $\Delta < 0$ is restricted to smaller values of $\kappa$ and $|\Delta|$ than previously, but its boundary remains qualitative the same. The smaller locking region for $\Delta > 0$ is bounded by a pitchfork (P) and two Hopf curves (H*), and it is almost vanishing for $\alpha = 0.3$ (see the inset in Figure 3(d)).

For $\alpha = 0.425$, neither of the two locking regions for $\Delta > 0$ is present in the bifurcation diagram (Figure 4(a)). The unbounded locking region has moved to very large values of

Copyright © by SIAM. Unauthorized reproduction of this article is prohibited.

$\kappa$ where the model validity is questionable, and the small locking region from the inset in Figure 3(d) has shrunk and disappeared so that the only relevant locking region is the one for $\Delta < 0$. Its conjugate-locking component forms a thin strip bounded by a pitchfork, a saddle-node, and two Hopf curves. The fixed-locking component is much larger, and its lower boundary involves a codimension-three bifurcation where a Hopf curve forms a cusp at the saddle-node-Hopf bifurcation point. This bifurcation marks the final qualitative change in the boundary of the fixed-locking region for $\alpha \leq 1$ and is discussed in more detail in section 4.4.2.

While the fixed-locking regions in Figures 4 (b)–(d) are qualitatively the same, they still undergo some important quantitative transitions. In particular, for $\alpha = 0.55$ (Figure 4(b)), the fixed-locking region crosses the $\Delta = 0$ line, making stable phase locking possible for both signs of $\Delta$ again (Figures 4(c)–(d)). The conjugate-locking region is qualitatively similar to that from Figure 4(a), but it has contracted in the $\Delta$ direction to a very thin strip that is hardly visible. For $\alpha = 0.6$ (Figure 4(c)) it shrinks to a tiny region to the right of the Bodganov–Takens point (BT$^*$) at $(\kappa, \Delta) \approx (22, -5)$ and vanishes for even higher values of $\alpha$ (Figure 4(d)). The key bifurcations responsible for the disappearance of the conjugate-locking region are discussed in section 4.4.2.

Finally, for $\alpha = 1$ (Figure 4(d)) there is only one locking region, and it is of fixed type. It is found for low values of the coupling strength, around $0 < \kappa < 10$, and has a rather wide extent in the frequency detuning, $-15 < \Delta < 10$. Starting at the origin and going counterclockwise, its boundary consists of a saddle-node curve (S), two Hopf curves (H), and a pitchfork curve (P). The changes in the boundary type occur via saddle-node-Hopf (SH), double-Hopf (HH), and pitchfork-Hopf (PH) bifurcations. For even higher values of $\alpha$, the locking region expands along the $\Delta$ direction, and its right boundary shifts towards the origin.

In summary, the bifurcation analysis of phase-locked solutions (4.17), presented in Figures 3 and 4, reveals a complicated web of codimension-one bifurcation curves in the $(\kappa, \Delta)$ plane from which we extracted those that form the backbone of the system dynamics and might be of interest for laser applications. The diagrams uncover an intricate structure of fixed- and conjugate-locking regions imposed by the $\mathbb{Z}_2$ symmetry. Both locking types are possible for sufficiently small $\alpha$, but a number of higher codimension bifurcations occur for $0 < \alpha < 1$ that drastically modify the shape, extent, and number of the locking regions. Ultimately, for sufficiently large $\alpha$, these bifurcations lead to just one (fixed) locking region, where the outer lasers are synchronized exactly in phase but are typically out of phase with the middle laser.

### 4.4.2. Bifurcations of codimension higher than two.

Following [30], we define the *codimension of a bifurcation* as the lowest dimension of a parameter space that contains the bifurcation in a persistent way. In the $(\kappa, \Delta)$ plane, we identify two types of bifurcation points of codimension higher than two: genuine codimension-three bifurcations, and extrema of codimension two bifurcation curves in the $(\alpha, \kappa, \Delta)$ space that are tangent to the $(\kappa, \Delta)$ plane. The former are artifacts of the two-dimensional section, meaning that they are of codimension two for a differently defined section. Nevertheless, such extrema result in qualitative changes to the locking regions in the $(\kappa, \Delta)$ plane that are important from the applications viewpoint.

A codimension-three triple-Hopf bifurcation for $\alpha \approx 0.0425$ alters the boundary of the locking region. The bifurcation diagram for $\alpha = 0.03$ in Figure 5(a) is representative of the

Copyright © by SIAM. Unauthorized reproduction of this article is prohibited.

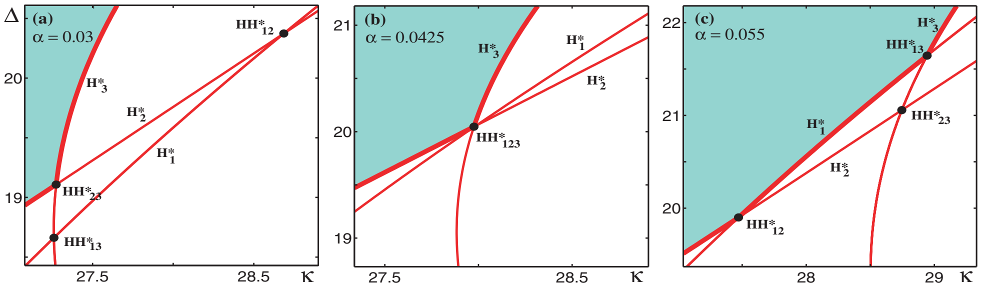

**Figure 5.** *Two-parameter bifurcation diagrams in the* $(\kappa, \Delta)$ *parameter plane showing an expanded view around the codimension-three triple-Hopf bifurcation point (*$HH^*_{123}$*). Curves represent codimension-one bifurcations, and black dots indicate where crossings and tangencies between different bifurcation curves give rise to codimension-two bifurcation points. For the labeling, color coding, and shading see Table* 3.

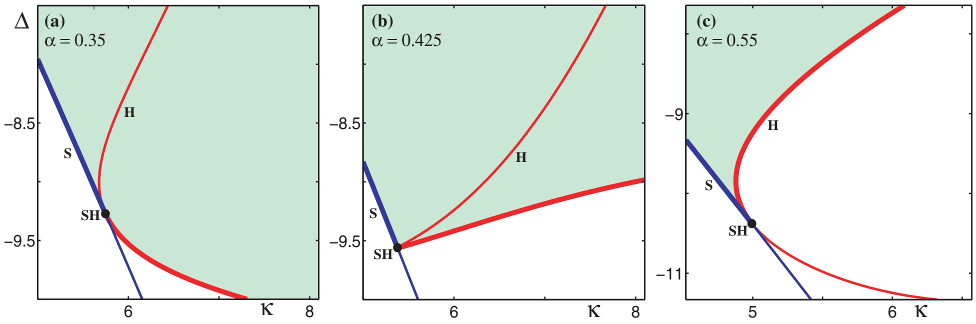

**Figure 6.** *Two-parameter bifurcation diagrams in the* $(\kappa, \Delta)$ *parameter plane showing an expanded view around the codimension-three saddle-node-Hopf bifurcation point (SH). Curves represent codimension-one bifurcations, and black dots indicate where crossings and tangencies between different bifurcation curves give rise to codimension-two bifurcation points. For the labeling and color coding, and shading see Table* 3. *For clarity each panel contains an inset with a sketch.*

situation close to, but before, the triple-Hopf bifurcation ($\mathrm{HH}^*_{123}$). Three different curves of Hopf bifurcation ($\mathrm{H}^*_1$, $\mathrm{H}^*_2$, and $\mathrm{H}^*_3$) involving conjugate equilibria intersect at three different codimension-two double-Hopf points ($\mathrm{HH}^*_{12}$, $\mathrm{HH}^*_{13}$, and $\mathrm{HH}^*_{23}$). In particular, $\mathrm{H}^*_2$ and $\mathrm{H}^*_3$ bound the conjugate-locking region and meet at the corner of this region at $\mathrm{HH}^*_{23}$. As $\alpha$ is increased, the three double-Hopf bifurcations move towards each other and meet when $\alpha \approx 0.0425$ at the triple-Hopf bifurcation ($\mathrm{HH}^*_{123}$ in Figure 5(b)). At this point, each of the two conjugate equilibria involved has three distinct pairs of purely imaginary eigenvalues. Past the codimension-three bifurcation, the three double-Hopf points move apart so that all three curves, $\mathrm{H}^*_1$, $\mathrm{H}^*_2$, and $\mathrm{H}^*_3$, bound the locking region with corners at $\mathrm{HH}^*_{12}$ and $\mathrm{HH}^*_{13}$ (Figure 5(c)). A comparison with the bifurcation analysis in Figure 3 reveals that Figures 3(a) and (b) are either side of the triple-Hopf bifurcation from Figure 5(b).

Another codimension-three bifurcation that alters the shape of the locking region is a saddle-node-Hopf cusp bifurcation for $\alpha \approx 0.425$, where a Hopf curve (H) has a cusp at the tangency point with a saddle-node curve (S). In all three panels of Figure 6 the locking region is bounded by saddle-node and Hopf bifurcation curves that are tangent at a saddle-node-

Copyright © by SIAM. Unauthorized reproduction of this article is prohibited.

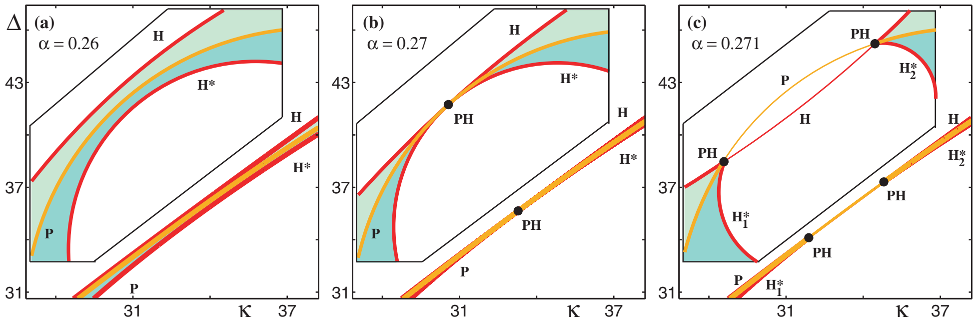

**Figure 7.** *Two-parameter bifurcation diagrams in the $(\kappa, \Delta)$ parameter plane showing an expanded view around the codimension-two-plus-one pitchfork-Hopf bifurcation point (PH). Curves represent codimension-one bifurcations, and black dots indicate where crossings and tangencies between different bifurcation curves give rise to codimension-two bifurcation points. For the labeling and color coding, and shading see Table 3. For clarity each panel contains an inset with a sketch.*

Hopf point (SH). A stable focus and a saddle-focus are created along the saddle-node curve on the boundary of the fixed-locking region. When moving in a clockwise direction about SH, the stable focus loses stability at a Hopf bifurcation. The locking boundary is smooth below the codimension-three point (Figure 6(a)). However, it becomes piecewise smooth at the codimension-three bifurcation, where the thin and thick branches of H form a cusp in order to swap their relative position (Figure 6(b)). The boundary remains piecewise smooth for higher values of $\alpha$ (Figure 6(c)). Such a codimension-three bifurcation is a transition between different unfoldings of a codimension-two saddle-node-Hopf bifurcation (unfolding numbers four and three in [42]) with a different type and location of complicated nonstationary dynamics originating from SH. We note that this bifurcation was identified as an important organizing center in optically injected lasers [83] and two-laser systems [81, 23].

As $\alpha$ is increased, the $(\kappa, \Delta)$ plane passes through an extremum of codimension-two bifurcation curves that form part of the locking boundary in the $(\alpha, \kappa, \Delta)$ parameter space. Such transitions explain the splitting of the locking region into separate parts in the $(\kappa, \Delta)$ plane and are illustrated with three examples below.

The first example is a minimum of a pitchfork-Hopf bifurcation curve at $\alpha \approx 0.27$. Just below the minimum, a stable fixed equilibrium from the fixed-locking region loses stability either via a Hopf or a supercritical pitchfork bifurcation along the curves H and P, respectively (Figure 7(a)). Likewise, a pair of stable conjugate equilibria created by the pitchfork bifurcation along P loses stability via a Hopf bifurcation along H$^*$. Increasing $\alpha$ causes the curves, H, H$^*$, and P, to move closer together. When $\alpha \approx 0.27$, the curves become tangent so that the locking region is pinched at a pitchfork-Hopf point (PH in Figure 7(b)). This point is a minimum of a pitchfork-Hopf curve in $(\alpha, \kappa, \Delta)$ space. Past the minimum, the curve H$^*$ splits into two disjoint branches, H$_1^*$ and H$_2^*$ (Figure 7(b)). These branches emanate from two pitchfork-Hopf bifurcations (PH) at the intersection points between P and H. Concurrently, the locking region (including its fixed and conjugate components) splits into two separate parts; compare with Figures 3(c)–(d).

The second example is a minimum of a Bogdanov–Takens bifurcation curve at $\alpha \approx 0.5699$. Just below the minimum, there is a single locking region where two stable conjugate equilibria

Copyright © by SIAM. Unauthorized reproduction of this article is prohibited.

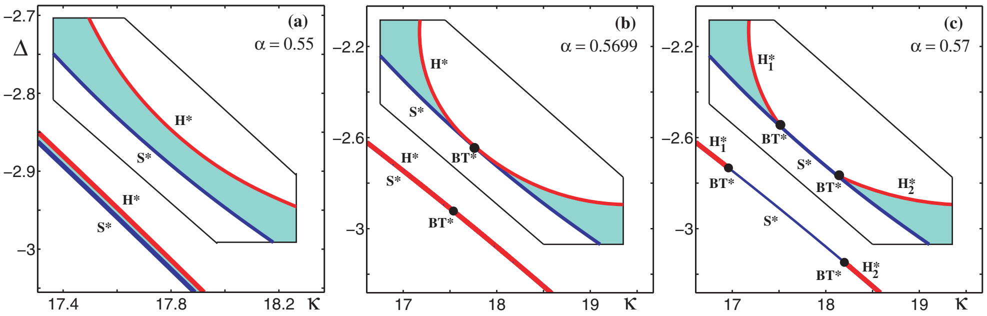

**Figure 8.** *Two-parameter bifurcation diagrams in the* $(\kappa, \Delta)$ *parameter plane showing an expanded view around the codimension-two-plus-one double Bogdanov–Takens bifurcation point (BT**). *Curves represent codimension-one bifurcations, and black dots indicate where crossings and tangencies between different bifurcation curves give rise to codimension-two bifurcation points. For the labeling, color coding, and shading see Table* 3*. For clarity each panel contains an inset with a sketch.*

are simultaneously created at saddle-node bifurcations along $S^*$ and lose stability in a Hopf bifurcation along $H^*$ (Figure 8(a)). When $\alpha \approx 0.5669$, the curves $S^*$ and $H^*$ become tangent at a Bogdanov–Takens point ($BT^*$ in Figure 8(b)). This point is a minimum of a Bogdanov–Takens curve in $(\alpha, \kappa, \Delta)$ space. Past the minimum, the curve $H^*$ splits into two disjoint branches, $H_1^*$ and $H_2^*$ (Figure 8(c)). These branches emanate from two $BT^*$ points at the corners of two separate locking regions; compare with Figures 4(b)–(c). Such a transition was also reported in a laser with time-delayed optical feedback [22].

Finally, we briefly describe an interesting bifurcation transition associated with the disappearance of the conjugate component of the locking region shown in Figure 4(a). For $\alpha = 0.57$, starting at the origin and moving counterclockwise (Figure 9(a)), the conjugate-locking component is bounded by a pitchfork curve (P), a pitchfork-saddle-node point ($PS^*$), a saddle-node curve ($S^*$), the Bogdanov–Takens point ($BT^*$) (not shown), and a Hopf curve ($H^*$) extending between BT and the origin. With increasing $\alpha$, the points $PS^*$ and $BT^*$ move toward the origin along P and H, respectively. The $PS^*$ point reaches the origin first, when $\alpha \approx 0.5773$ (Figure 9(b)). The conjugate-locking component (too thin to be visible in Figure 9(b)) vanishes as H shrinks due to the $BT^*$ point moving into the origin and colliding with its symmetric counterpart (found for $\kappa < 0$) at a maximum of a Bogdanov–Takens curve in $(\alpha, \kappa, \Delta)$ space. Concurrently, the thin and thick branches of P switch their relative position and $PS^*$ moves away from the origin along the thin branch of P (Figure 9(c)).

### 4.5. Locking-unlocking transitions and global bifurcations.

So far, higher codimension bifurcations of equilibria have been described as evidence for changes in the type and shape of the locking boundary. Such bifurcations play another very important role—they act as *organizing centers* [82] linking different types of nonstationary behavior that are usually found in the vicinity of the locking regions but can also coexist with a stable equilibrium [42]. A different approach to studying laser dynamics involves Lyapunov exponent calculations [12, 8, 47]. In this section, we combine bifurcation analysis and Lyapunov exponent calculations to study (global) bifurcations and the ensuing multistability involved in the locking-unlocking transitions near certain codimension-two bifurcations. Because of our interest in modern laser applications and the effects of shear, we focus here on semiconductor lasers and $\alpha = 2$.

Copyright © by SIAM. Unauthorized reproduction of this article is prohibited.

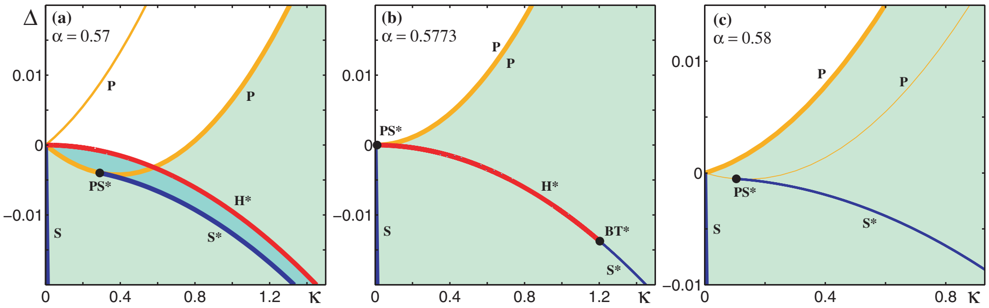

**Figure 9.** *Two-parameter bifurcation diagrams in the* $(\kappa, \Delta)$ *parameter plane showing the bifurcations involved in the disappearance of a conjugate-locking region (dark green). Curves represent codimension-one bifurcations, and black dots indicate where crossings and tangencies between different bifurcation curves give rise to codimension-two bifurcation points. For the labeling, color coding, and shading see Table 3.*

Figure 10 gives a broad overview of the systems dynamics for weak coupling. The locking region boundary is formed by saddle-node (S), pitchfork (P), and Hopf (H) bifurcations (Figure 10(a)), and it is qualitatively similar to the boundary found in Figure 4(d) for $\alpha = 1$. A comparison between Figures 10(a)–(b) shows that Lyapunov exponent calculations "fail" to recover parts of the locking region obtained from bifurcation analysis. This mismatch is a clear indication of bistability and can be explained by global homoclinic and heteroclinic bifurcations not studied in section 4.4.

**4.5.1. Negative Δ and homoclinic bifurcations.** It turns out that a part of the saddle-node bifurcation (S) bounding the locking region at negative Δ in Figure 10(a) is of global type. It emanates from the origin as a saddle-node homoclinic bifurcation [42, Chap. 7], Shom in Figure 10(c), where a codimension-one homoclinic orbit is tangent to the neutral eigendirection of a nonhyperbolic saddle-node equilibrium. In other words, the saddle-node bifurcation takes place on a limit cycle. At the codimension-two noncentral saddle-node homoclinic bifurcation [14, 20] (NC), Shom changes to a local saddle-node bifurcation (S) and meets a codimension-one homoclinic orbit to a saddle-focus bifurcation (hom). Starting from NC, hom extends above S, cutting through the tip of the locking region (Figure 10(c)). On approaching the locking region from below and to the right of the NC point, the saddle-node bifurcation occurs before the homoclinic bifurcation, i.e., it no longer takes place on a limit cycle. Inside the tip of the locking region, the stable equilibrium coexists with (complicated) nonstationary dynamics associated with infinite bifurcation cascades that accumulate onto hom and are described in more detail in Figure 12. Homoclinic orbits Shom and hom are fixed because they are contained within $\mathrm{Fix}(\mathbb{Z}_2)$.

The type of dynamics found near hom depends crucially on the saddle index [84, Chap. 3.2]:

$$\delta \equiv \frac{\Re(\lambda_s)}{\Re(\lambda_u)}, \tag{4.20}$$

where $\Re(\lambda_u)$ and $\Re(\lambda_s)$ are the real parts of the stable and unstable central eigenvalues of the saddle-focus, respectively. The part of hom between NC and $\delta_{-1}$ is the "tame" Shilnikov case with $\delta < -1$, where the homoclinic orbit bifurcates into a stable limit cycle found below

Copyright © by SIAM. Unauthorized reproduction of this article is prohibited.

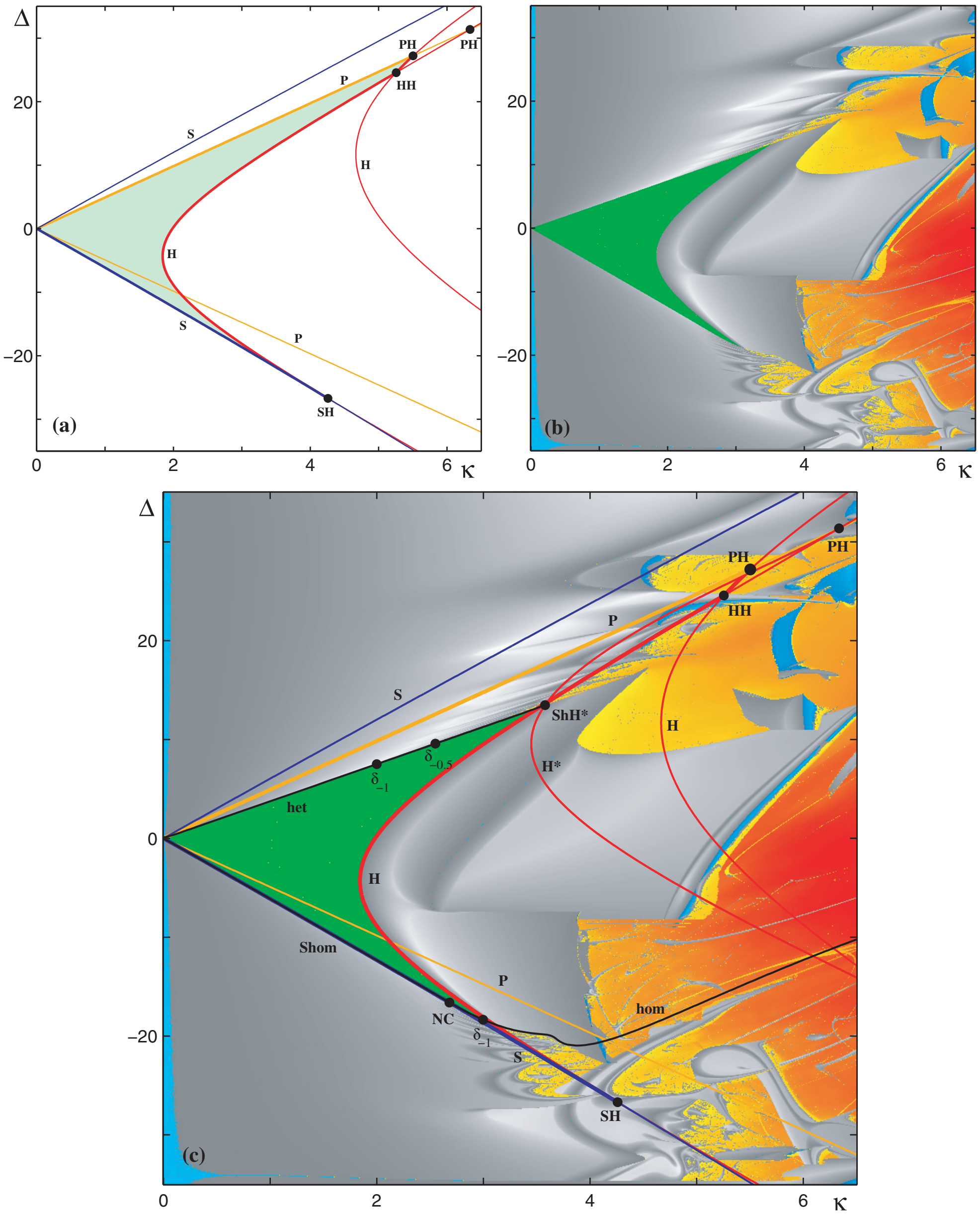

**Figure 10.** (a) *Bifurcation diagram,* (b) *Lyapunov diagram for increasing* $\kappa$*, and* (c) *both superimposed in the* $(\kappa, \Delta)$ *parameter plane for* $\alpha = 2$*. For the labeling and color coding see Tables* 2 *and* 3*.*

hom. The point $\delta_{-1}$ defined by $\delta = -1$ is a codimension-two Belyakov bifurcation [6] that marks the transition between the "tame" and "chaotic" Shilnikov cases. In the "chaotic" Shilnikov case, one expects complicated dynamics owing to the existence of infinitely many limit cycles of arbitrary period sufficiently close to hom. Figure 11 shows a one-parameter bifurcation diagram for the "chaotic" case with fixed $\kappa = 3.229$ and varied $\Delta$, together with examples of limit cycles converging to the homoclinic orbit. For $-1 < \delta < 0$ the theory

Copyright © by SIAM. Unauthorized reproduction of this article is prohibited.

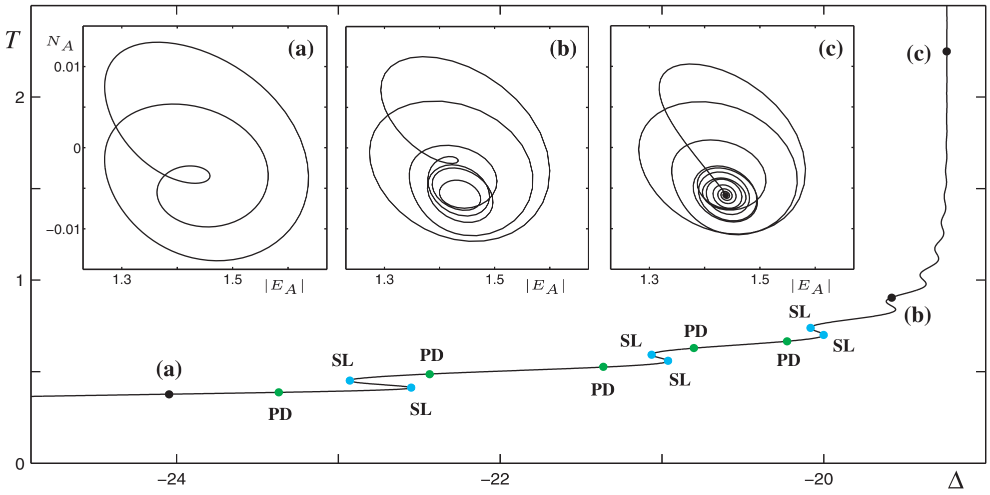

**Figure 11.** *One-parameter bifurcation diagram showing the period, $T$, of limit cycles vs. $\Delta$ on approaching the homoclinic bifurcation. Panels* (a)–(c) *show examples of limit cycles in projection onto the* $(|E_A|, N_A)$ *plane. The dots indicate first steps in the infinite cascade of saddle-node of limit cycles (SL) and period-doubling (PD) bifurcations. The parameter values are as follows:* $\alpha = 2$, $\kappa = 3.229$, (a) $(\Delta, T) = (-24.046, 0.377)$, (b) $(\Delta, T) = (-19.580, 0.906)$, *and* (c) $(\Delta, T) = (-19.239, 2.25)$.

predicts infinitely many turning points along a branch of limit cycles, corresponding to saddle-node of limit cycle bifurcations (SL). As the period, $T$, of the limit cycles tends to infinity, the characteristic "Shilnikov wiggles" converge from each side to the homoclinic bifurcation. Furthermore, if $-1 < \delta < -0.5$, the node cycles are born stable at SL but may lose stability via period-doubling bifurcations (PD). The bifurcation structure in the $(\kappa, \Delta)$ plane is shown in an expanded view around the bottom corner of the locking region in Figure 12(a). We computed cascades of saddle-node of limit cycle (SL) and period-doubling (PD) bifurcation curves that accumulate onto the "chaotic" part of hom. In particular, codimension-two cusp points on the SL curves and folds of the PD curves accumulate onto the Belyakov point, $\delta_{-1}$. Furthermore, each of the PD curves involves (infinitely many) secondary period doublings (not shown in the figure). Lyapunov exponent calculations in Figures 12(b)–(c) reveal that such accumulating cascades of SL and PD curves give rise to accumulating regions of *homoclinic chaos* [4, 2] that extend relatively far away from hom (see Figures 15(a)–(b) for an example of such a chaotic attractor).

It is worth noting that another region of chaos, found in the upper-right corner in Figures 12(b)–(c), is associated with a breakup of an invariant torus. The torus bifurcation curve (T) extends between the saddle-node-Hopf bifurcation point (SH) and the 1:2 resonance point. Along T, a stable limit cycle created at the Hopf bifurcation involved in SH bifurcates with a stable torus. The Lyapunov exponent calculations in Figures 12(b)–(c) reveal quasi-periodic oscillations, some of the infinitely many Arnold tongues [42, Chap. 7] with periodic dynamics, and large regions of chaos to the right of T.

**4.5.2. Positive Δ and heteroclinic bifurcations.** A considerable difference in the locking region between Figures 10(a)–(b) is found for positive $\Delta$. This difference is due to a heteroclinic bifurcation [42, Chap. 6], het in Figure 10(c). Along het, two codimension-one conjugate

Copyright © by SIAM. Unauthorized reproduction of this article is prohibited.

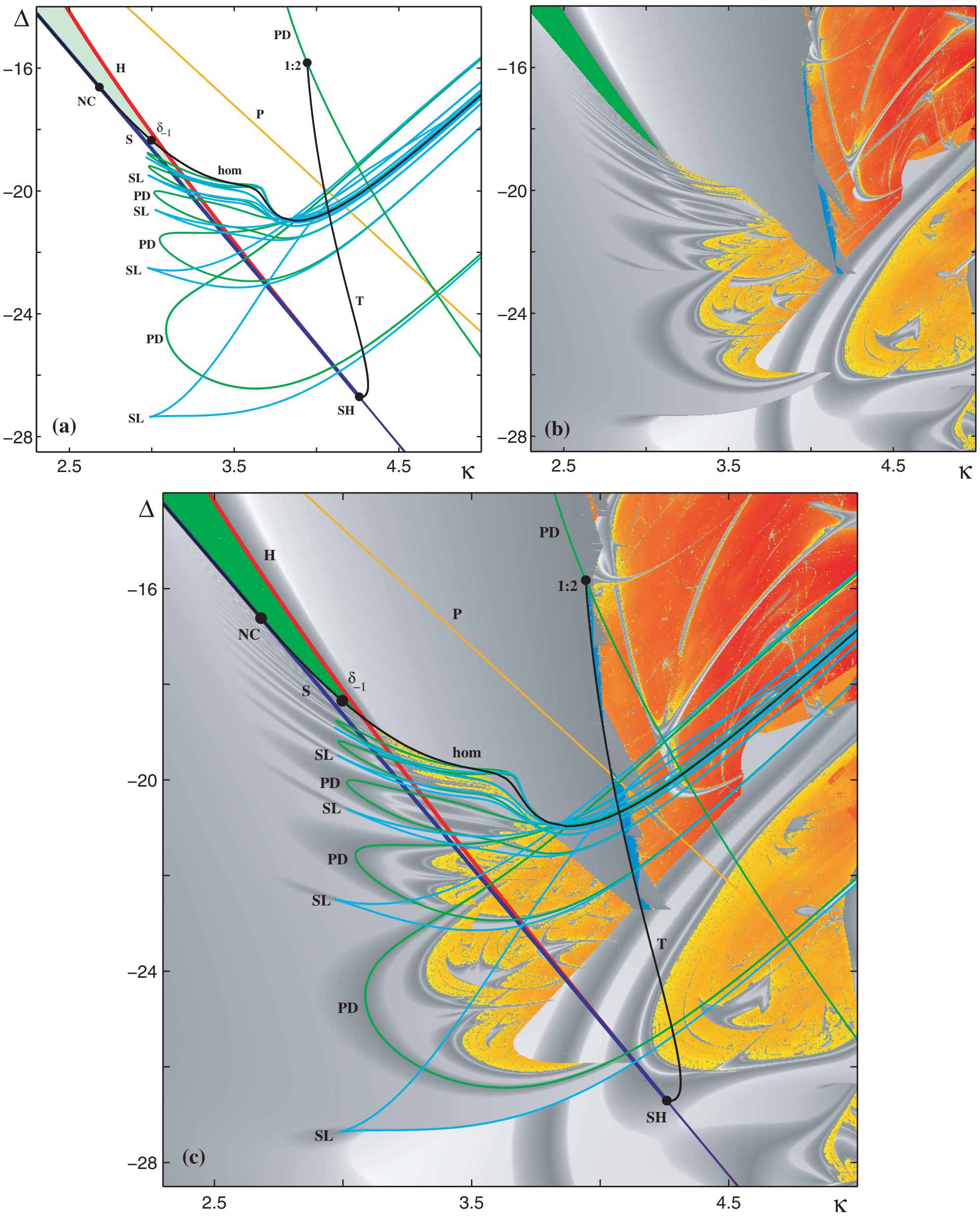

**Figure 12.** *An expanded view of the* $(\kappa, \Delta)$ *parameter plane from Figure* 10 *around the noncentral saddle-node homoclinic bifurcation point (NC) showing* (a) *bifurcation diagram,* (b) *Lyapunov diagram for increasing* $\kappa$*, and* (c) *both superimposed for* $\alpha = 2$*. The plots highlight complicated dynamics near the locking region (green) due to a self-similar cascade of period doublings and saddle-node of limit cycles associated with the homoclinic bifurcation (hom). For the labeling and color coding see Tables* 2 *and* 3.

heteroclinic connections between two conjugate saddles form a nonrobust and symmetric (i.e., $R_{\mathbb{Z}_2}$-invariant) heteroclinic cycle. An individual heteroclinic connection within the cycle is a *relative homoclinic connection*, meaning that it is a homoclinic connection to a saddle in the $\mathbb{Z}_2$ group orbit space. Hence, Shilnikov theorems for homoclinic bifurcations should apply

Copyright © by SIAM. Unauthorized reproduction of this article is prohibited.

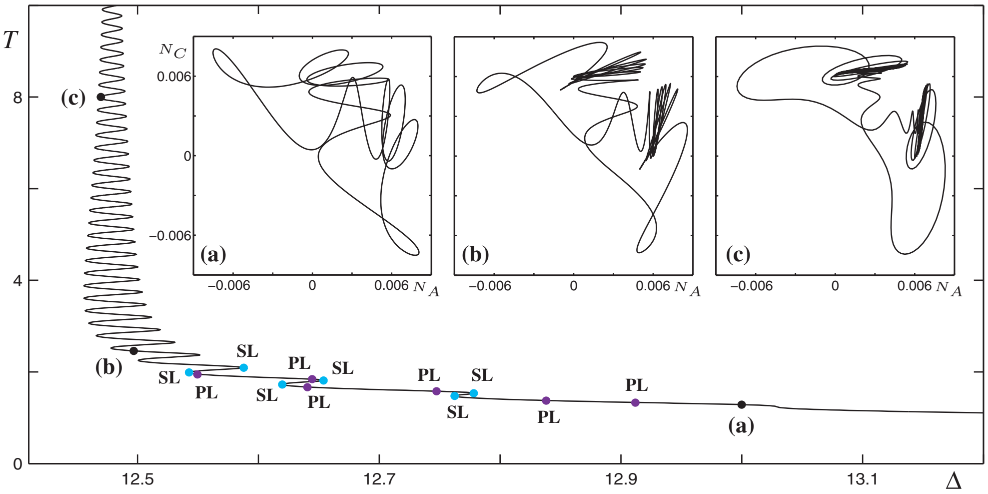

**Figure 13.** *One-parameter bifurcation diagram showing the period, $T$, of limit cycles vs. $\Delta$ on approaching the heteroclinic bifurcation. Panels* (a)–(c) *show examples of limit cycles in projection onto the $(N_A, N_C)$ plane. The dots indicate first steps in the infinite cascade of saddle-node of limit cycle (SL) and pitchfork of limit cycle (PL) bifurcations. The parameter values are as follows: $\alpha = 2$, $\kappa = 3.321875$,* (a) $(\Delta, T) = (13, 1.286)$, (b) $(\Delta, T) = (12.497, 2.459)$, *and* (c) $(\Delta, T) = (12.470, 8)$.

here. The curve het emanates from the origin and involves simple saddles that become saddle-foci at $\kappa \approx 1$. Along the "tame" part of het, the homoclinic orbit bifurcates into a stable limit cycle that is found above het. The het curve changes its type from "tame" to "chaotic" through a codimension-two Belyakov bifurcation ($\delta_{-1}$) and meets a curve of Hopf bifurcations ($\mathrm{H}^*$) at a codimension-two relative Shilnikov–Hopf bifurcation point ($\mathrm{ShH}^*$) [35, 11]. At $\mathrm{ShH}^*$ both conjugate saddles within the heteroclinic cycle undergo a Hopf bifurcation giving rise to a heteroclinic cycle with four point-to-orbit connections.

Figure 13 shows a one-parameter bifurcation diagram for the "chaotic" case with fixed $\kappa \approx 3.322$ and varied $\Delta$, together with examples of limit cycles converging to the heteroclinic orbit. As the period of the limit cycles, $T$, tends to infinity, the characteristic "Shilnikov wiggles" that involve a cascade of saddle-node of limit cycle bifurcations (SL) converge from each side to the heteroclinic bifurcation as in Figure 11. The slower rate of convergence that decreases towards $\mathrm{ShH}^*$ is a consequence of imaginary parts of the central stable complex conjugate eigenvalues being large compared to the real part of the leading unstable eigenvalue [84, Chap. 3.2]. An important difference from the homoclinic bifurcation is the absence of period-doubling bifurcations on the branch of limit cycles plotted in Figure 13. This is because the limit cycles created in the saddle-node bifurcations (SL) are symmetric, and according to equivariant bifurcation theory they cannot period double [42, Chap. 7.4]. Such cycles can undergo only saddle-node, pitchfork, and torus bifurcations, and so the period-doubling bifurcations from Figure 11 are replaced by a cascade of pitchfork bifurcations in Figure 13. In the $(\kappa, \Delta)$ plane, we calculated cascades of saddle-node of limit cycle (SL) and pitchfork of limit cycle (PL) bifurcation curves that accumulate onto the "chaotic" part of het (Figure 14(a)). Lyapunov exponent calculations in Figures 14(b)–(c) reveal that cascades of SL and PL curves are associated with a self-similar cascade of chaotic regions that too accumulate on het. In

Copyright © by SIAM. Unauthorized reproduction of this article is prohibited.

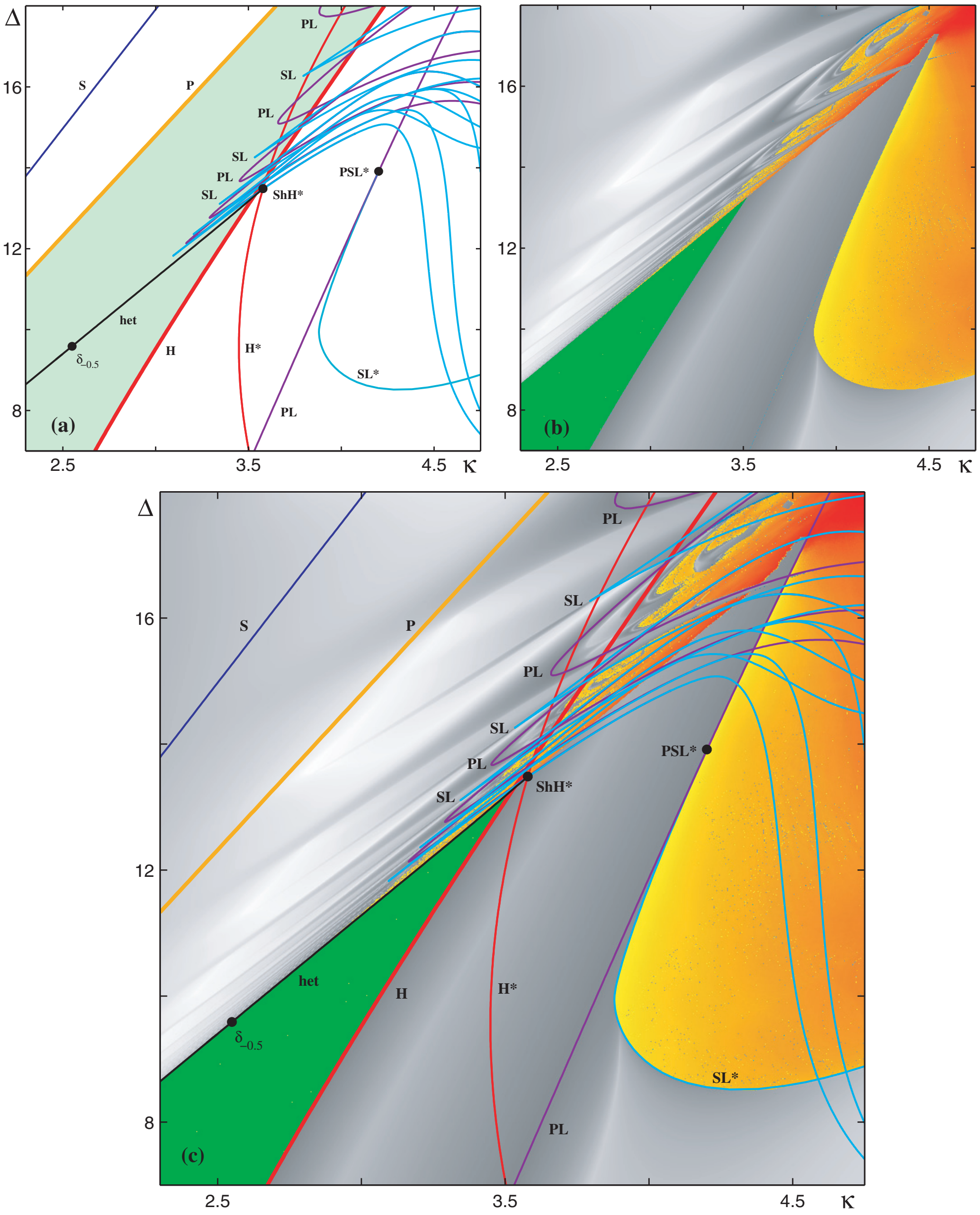

**Figure 14.** *An expanded view of the* $(\kappa, \Delta)$ *parameter plane from Figure* 10 *around the relative Shilnikov–Hopf point (ShH*) showing* (a) *bifurcation diagram,* (b) *Lyapunov diagram for increasing* $\kappa$, *and* (c) *both superimposed for* $\alpha = 2$. *The plots highlight a difference in the locking region (green) revealed by the bifurcation analysis and the Lyapunov exponent computations which is due to the heteroclinic bifurcation (het). For the labeling and color coding see Tables* 2 *and* 3.

particular, chaos is found to the right of the PL curves in Figure 14(c), where two conjugate limit cycles bifurcate from the symmetric limit cycle in a pitchfork bifurcation and then undergo a period-doubling cascade to *heteroclinic chaos* (see Figures 15(c)–(d) for an example of such a chaotic attractor).

Copyright © by SIAM. Unauthorized reproduction of this article is prohibited.

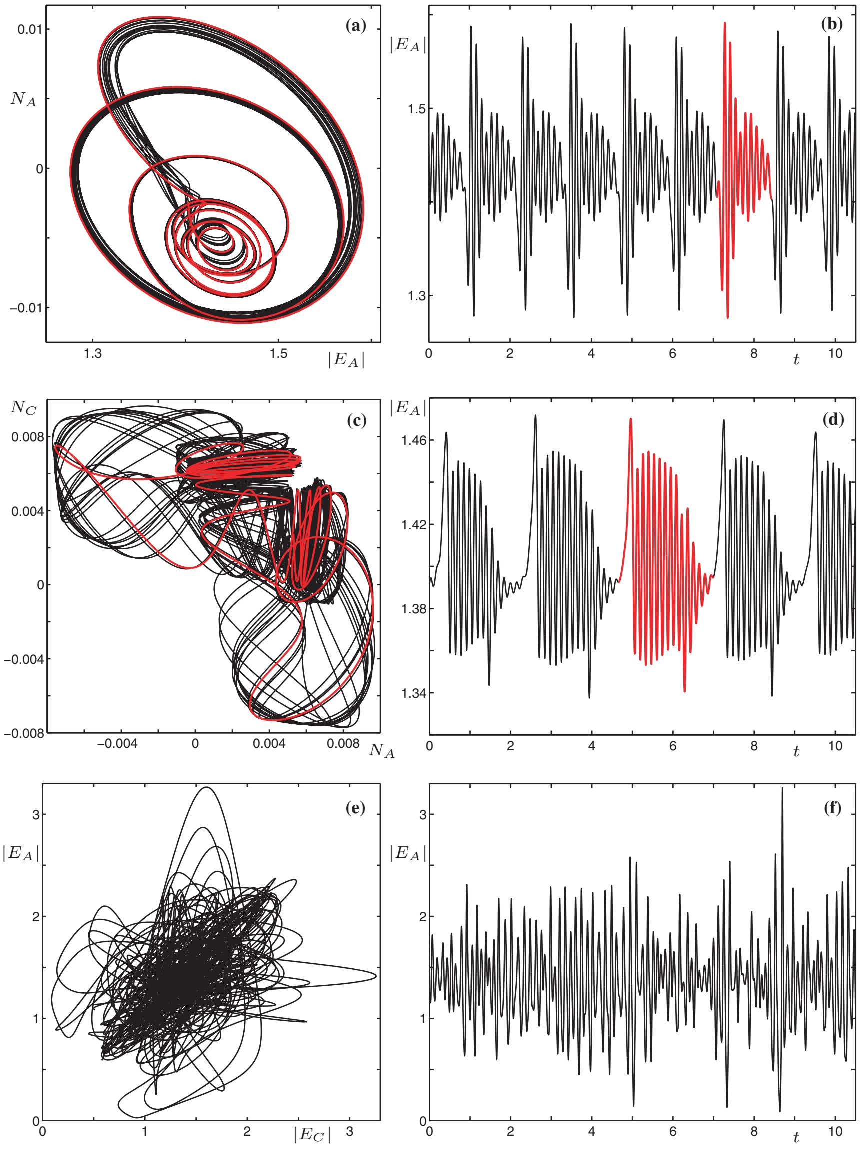

**Figure 15.** *Examples of different chaotic attractors for the coupled-laser equations* (4.2) *and* (4.8) *with* $\alpha = 2$ *shown as two-dimensional phase space projections (left column) and the corresponding time series of* $|E_A|$ *(right column). For* (a)–(b) $(\kappa, \Delta) = (3.229, -19.2804)$*;* (c)–(d) $(\kappa, \Delta) = (3.321875, 12.5275)$*; and* (e)–(f) $(\kappa, \Delta) = (10, 0)$*. Approximations to the largest Lyapunov exponents are* 0.18*,* 1.22*, and* 10.7*, respectively.*

It is worth noting another chaotic region in Figure 14(c) that does not seem to be related to het. This region has hardly visible periodic windows on the scale chosen here, and its boundary aligns with bifurcations of limit cycles (Figure 14(c)). Starting from the top, the boundary aligns with a subcritical pitchfork bifurcation (PL) and then changes to saddle-node bifurcation (SL) at the codimension-two pitchfork-saddle-node of limit cycle bifurcation (PSL*). Both boundary types correspond to an intermittent transition between periodic oscillations and chaos [55, Chap. 8.2].

Copyright © by SIAM. Unauthorized reproduction of this article is prohibited.

The overall picture is that the two global bifurcation curves roughly split the locking region into three parts. The middle part is comprised of monostable locking with the exception of small regions near the curves het and hom. The upper and lower parts are multistable, meaning that they involve an additional attractor(s) that coexists with the stable equilibrium. In the vicinity of the locking region there are a number of chaotic regions associated with different bifurcation scenarios. Specifically, we identified accumulating cascades of period doublings near hom and het, breakup of invariant tori born along the bifurcation curve originating from the saddle-node-Hopf bifurcation on the locking boundary, and (intermittent) limit cycle to chaos transitions due to subcritical pitchfork and saddle-node bifurcations of limit cycles.

**4.6. Coupling-induced chaotic attractors.** A solitary single-mode class-B laser can be described by the rate equations

$$\frac{d|E|}{dt} = \beta\gamma N|E|, \tag{4.21}$$

$$\frac{d\varphi}{dt} = -\alpha\beta\gamma N - (\Omega - \nu), \tag{4.22}$$

$$\frac{dN}{dt} = \Lambda - (N+1) - (1+\beta N)|E|^2, \tag{4.23}$$

which define a three-dimensional dynamical system with $\mathbb{S}^1$ symmetry. Since the $\mathbb{S}^1$ group orbit space is just two-dimensional ((4.22) decouples from (4.21) and (4.23)), the single-laser model cannot admit chaotic solutions. The equilibrium, at the origin of the complex $E$-plane, is globally stable for $0 < \Lambda < 1$ and turns unstable via a supercritical Hopf bifurcation (if $\Omega - \nu \neq 0$) when $\Lambda = 1$. The stable limit cycle exists for $\Lambda > 1$ as a unique asymptotically stable attractor.

However, it has been well established, both experimentally and theoretically, that a class-B laser can display a variety of instabilities and chaos in response to external perturbations [71]. Complex nonlinear dynamics and chaos have been reported for $\alpha$ large enough, but very little or no chaos at all have been found for $\alpha \sim 0$ [41]. The same is true for the three-laser system at hand, where for $\alpha$ sufficiently large, extensive regions of chaos appear in the parameter space (Figure 2). Figure 15 shows three examples of chaotic attractors with different topologies. The first example (Figures 15(a)–(b)) is found close to a homoclinic bifurcation. Its shape resembles the homoclinic orbit, and such an attractor is often referred to as *homoclinic chaos*. The shape of the chaotic attractor in the second example resembles the shape of the nearby heteroclinic orbit (Figures 15(c)–(d)), and such an attractor is often referred to as *heteroclinic chaos*. The third example is quite different from the first two in that it does not seem to resemble any regular shape at all (Figures 15(e)–(f)). Previous studies and previous sections of this paper focus on different approaches to quantifying externally induced chaotic attractors (for example, Lyapunov exponent calculations, bifurcation, or asymptotic analysis), but little is understood as to why they appear. From an applications viewpoint, this question is of interest for the analysis of large arrays of semiconductor lasers, where the parameter space is largely dominated by chaotic attractors and their bifurcations. We now identify the special properties of the laser phase space and of the external perturbation that may produce chaos.

In their recent work, Wang and Young [76] prove that, when *suitably* perturbed, any stable hyperbolic limit cycle can be turned into "observable" chaos (a strange attractor). This result

Copyright © by SIAM. Unauthorized reproduction of this article is prohibited.

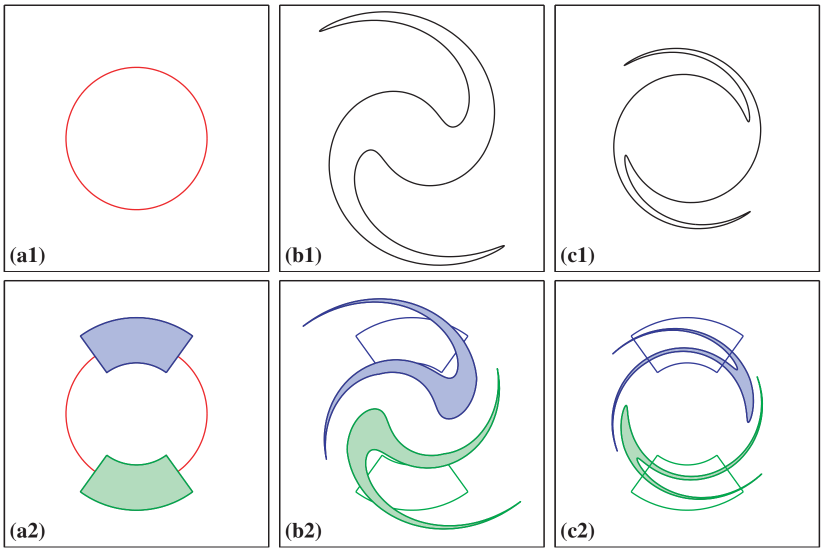

**Figure 16.** *Time evolution of sets of initial conditions showing the creation of horseshoes in the phase space of a suitably kicked oscillator with no shear. The sets of initial conditions are (top) the stable red circle and (bottom) the blue and green sets containing parts of the circle. Shown are phase portraits* (a) *before and* (b)–(c) *after the first kick.*

is derived for periodic but discrete-time perturbations (kicks) that deform the stable limit cycle of the unkicked system. The key concept is the creation of Smale horseshoes [68] via a stretch-and-fold action due to an interplay between the kicks and the local geometry of the phase space. Depending on the degree of shear, quite different kicks are required to create a stretch-and-fold action and horseshoes. Intuitively, it can be described as follows. In systems without shear, where points in phase space rotate with the same angular frequency independent of their distance from the origin, the kick alone has to create the stretch-and-fold action. This is demonstrated in Figure 16. Horseshoes are formed ((a2)–(c2)) as the system is suitably kicked in both radial and angular directions ((b1)–(b2)) and then relaxes back to the attractor (red curve) of the unkicked system ((c1)–(c2)). Repeating this process reveals chaotic invariant sets; however, whether or not a specific kick results in "observable" chaos is a nontrivial task requiring the techniques developed in [75]. In the presence of shear, where points in phase space rotate with different angular frequencies depending on their distance from the origin, the kick does not have to be so specific or carefully chosen. In fact, it may be sufficient to kick nonuniformly in the radial direction alone and rely on natural forces of shear to provide the necessary stretch-and-fold action.

These effects are illustrated in a single laser model (4.21)–(4.23) with nonuniform kicks in the radial direction alone for $\alpha = 0$ (no shear) and $\alpha = 2$ (shear) in Figure 17. When $\nu = \Omega$, there is a stable circle of nonhyperbolic equilibria which we plot in red and refer to as $\Gamma$. Kicks modify the electric field amplitude, $|E|$, by a factor of $0.8\sin(4\varphi)$ at times $t = 0,\ 0.25,\ 0.5,$ and $0.75$ but leave the phase, $\varphi$, unchanged. For $\alpha = 0$ each point on the black curve spirals onto $\Gamma$ in time but remains in the same radial plane defined by a constant phase $\varphi = \varphi(0)$. Hence, the black curve does not have any folds at any time. However, for

Copyright © by SIAM. Unauthorized reproduction of this article is prohibited.

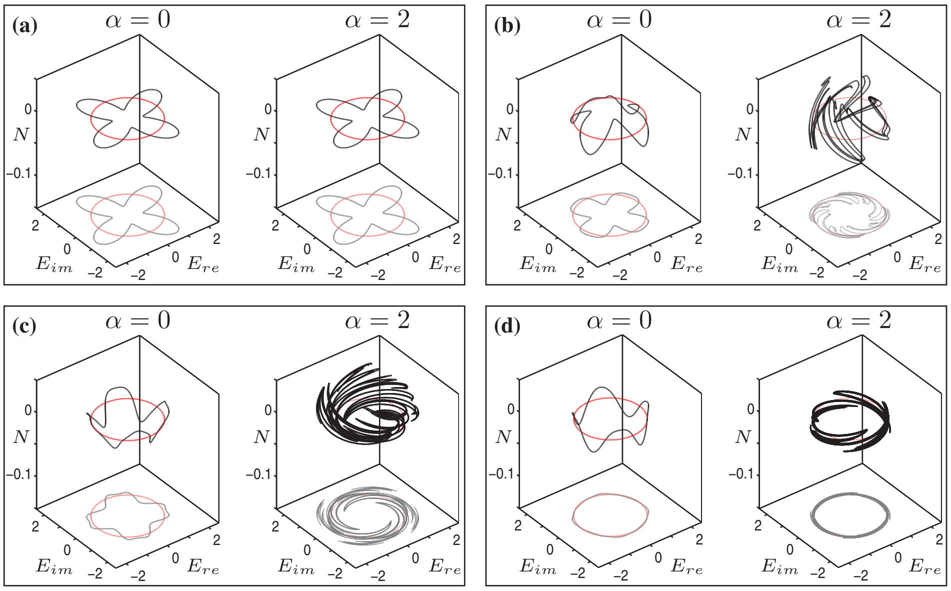

**Figure 17.** *Snapshots at times* (a) $t = 0$, (b) $t = 0.28$, (c) $t = 0.56$, *and* (d) $t = 1$ *showing the time evolution (black curve) of* 15000 *initial conditions, initially distributed equally over the stable red circle* $\Gamma$, *in the solitary-laser model* (4.21)–(4.23) *with kicks applied at* $t = 0, 0.25, 0.5, 0.75$. *A comparison between* $\alpha = 0$ *and* $\alpha = 2$ *illustrates the* $\alpha$*-induced stretch-and-fold action in the laser phase space. See the electronic supplementary material (*81738_01.gif*) for the full-time simulation.*

$\alpha = 2$, points on the black curve with larger amplitudes, $|E(t)|$, rotate with larger angular frequencies. This gives rise to an intricate stretch-and-fold action that is strongly enhanced by the spiralling transient motion about $\Gamma$ [80]. Folds and horseshoes are formed under the evolution of the flow even though the kicks are in the radial direction alone; see the electronic supplementary material (81738_01.gif) for a full-time simulation.

It is important to note that the rigorous results for turning stable limit cycles into chaotic attractors are derived for periodic and discrete-time perturbations. Coupled laser systems have continuous-time perturbations that may not be periodic, meaning that the analysis in [76] cannot be applied to our problem directly. Nonetheless, it gives a new valuable insight as to why vast regions of chaos appear for $\alpha$ sufficiently large. Additionally, it shows that creating "observable" chaos for $\alpha = 0$ may be difficult but not impossible because lasers are perturbed in both radial and angular directions (see equations (4.8)). In fact, we have found small regions of chaos in linear arrays of more than five lasers with $\alpha = 0$.

## 5. Composite-cavity mode model.

In the previous section we discussed the coupled-laser model (4.1)–(4.2) based on the field expansion (3.2) in terms of passive optical modes of the *uncoupled* lasers. Such an ODE model is relatively simple, independent of the physical coupling realization (side-to-side or face-to-face), but limited to weak coupling between lasers. This section discusses the composite-cavity mode model that approximates more accurately the electromagnetic wave equation (3.1) and is valid for any coupling between the lasers [65, 16]. As such, it serves as a benchmark against which the simpler coupled-laser model can be compared.

Copyright © by SIAM. Unauthorized reproduction of this article is prohibited.

In the composite-cavity mode approach, laser coupling is fully included in solving the homogeneous wave equation (3.1). The solutions $U_j(\mathbf{r})$ are then the passive optical modes for the *entire* coupled-laser system, and they are referred to as *composite-cavity modes* [15, 64, 65, 81, 23] or *supermodes* [38]. Nonlinear interactions between composite-cavity modes rather than individual lasers is the main conceptual difference from the coupled-laser approach. The composite-cavity mode approach can describe both physical realizations of optical coupling from Figure 1 [17, Chap. 7-6]. However, each physical realization has to be treated as a separate problem because it will involve a different refractive-index function, $n(\mathbf{r})$, and different boundary conditions.

Here, we consider three single-mode lasers coupled side to side (Figure 1(a)). The lasers have the shape of rectangular bars of widths $w_A = w_C = 4$ $\mu$m and they $w_B = (4 + \Delta w)$ $\mu$m, and they are placed a distance, $d$, apart in the $x$ direction. They have the same height, $h$, in the $y$ direction and the same length, $L$, in the $z$ direction [24]. To simplify the analysis, we follow [17, Chap. 7-6] and use the effective index approximation to give

$$U_j(\mathbf{r}) = X_j(x)\, Y(x, y)\, Z(z),$$

where $Y$ has a weak dependence on $x$. Then, we focus on a one-dimensional Helmholtz equation for the $x$ direction,

$$\left[ \frac{\partial^2}{\partial x^2} + n_{eff}^2(x) \frac{\Omega_j^2}{c^2} - k_z^2 \right] X_j(x) = 0, \tag{5.1}$$

which follows from (3.5). The effective refractive index, $n_{eff}(x)$, differs slightly from the actual refractive index, $n(x)$, and we assume a piecewise constant function

$$n_{eff}(x) = \begin{cases} n_l = 3.61 & \text{in lasers } A, B, \text{ and } C, \\ n_g = 3.6 & \text{outside the lasers.} \end{cases} \tag{5.2}$$

The electromagnetic theory requires that $X_j(x)$ and its first derivative with respect to $x$ be continuous at each laser boundary defined by a discontinuity in the effective refractive index. Additionally, we require that $X_j(x)$ tend to zero as $x \to \pm\infty$. As in [24], we seek analytical solutions $X_j(x)$ to (5.1) in the form of sine and cosine functions within the lasers and exponential decays outside the lasers. Given such boundary conditions, the solutions $X_j(x)$ satisfy the orthogonality relation

$$\int_{-\infty}^{\infty} n_{eff}^2(x) X_j(x) X_{j'}(x) dx = \delta_{jj'} \mathcal{N}_x, \tag{5.3}$$

where we choose the normalization constant

$$\mathcal{N}_x = \frac{n_g^2}{2}(3w_0 + 2d_0),$$

with $w_0 = 4\mu$m and $d_0 = 4\mu$m. Furthermore, we assume a standing wave solution in the $z$ direction,

$$Z(z) = \sin(k_z z) \quad \text{for} \quad z \in [0, L],$$

Copyright © by SIAM. Unauthorized reproduction of this article is prohibited.

where $L = j\pi/k_z$, $j$ is an integer, and $k_z = 5\pi \times 10^6$ m$^{-1}$ is the $z$ component of the total wavevector

$$k_j = \frac{\Omega_j}{c} = \sqrt{k_{x,j}^2 + k_y^2 + k_z^2}.$$

The component $Y(x,y)$ is obtained separately for a laser bar and passive sections outside lasers (hence the weak dependence on $x$), and $Y(x,y)$ tends to zero as $y \to \pm\infty$ [17].

Given $U_j(\mathbf{r})$, one can substitute the expansion (3.2) into the inhomogeneous wave equation (3.1) and use (3.7) to obtain a set of ODEs for the time evolution of the normalized composite-cavity mode amplitudes, $E_j(t)$ [23]:

$$\frac{dE_j}{dt} = -[i(\Omega_j - \nu) + \gamma]E_j + \gamma \sum_{j'} \left\{ \sum_s K_{jj'}^s \left[(1 + \beta N_s) - i\alpha\beta(1 + N_s)\right] \right\} E_{j'}. \tag{5.4}$$

The normalized population inversion, $N_s$, in laser $s = A$, $B$, $C$ evolves accordingly to [23]:

$$\frac{dN_s}{dt} = \Lambda - (N_s + 1) - \sum_{j,j'} K_{jj'}^s (1 + \beta N_s)\mathrm{Re}[E_j \overline{E}_{j'}]. \tag{5.5}$$

Clearly, (5.4)–(5.5) describe nonlinear interactions of composite-cavity modes rather than individual lasers. The model has no limitations on the coupling strength as different composite-cavity modes become the modes of a single large-area laser in the limit of maximum coupling given by $d \to 0$. Another difference from the coupled-laser model is that physical coupling parameters such as the laser distance, $d$, and the laser width difference, $\Delta w$, enter (5.4)–(5.5) implicitly via the 18 modal integrals

$$K_{jj'}^s = \frac{n_l^2}{\mathcal{N}} \int_s U_j(\mathbf{r}) U_{j'}(\mathbf{r}) d\mathbf{r} = \Gamma \frac{n_l^2}{\mathcal{N}_x} \int_s X_j(x) X_{j'}(x) dx. \tag{5.6}$$

Here, the integration extends over the volume ($d\mathbf{r}$) or width ($dx$) of the respective laser $s$ with the effective refractive index, $n_l$. The confinement factor, $\Gamma$, quantifies the normalized overlap between a passive composite-cavity mode and a laser $s$ in the $y$ and $z$ directions. From a physics viewpoint, a diagonal element, $K_{jj}^s$, quantifies the spatial contribution from laser $s$ to the amplification and $\alpha$-induced frequency shift of mode $j$. An off-diagonal element, $K_{j\neq j'}^s$, quantifies the spatial contribution to nonlinear interactions between composite-cavity modes $j$ and $j'$ within laser $s$ (resulting in coupling-induced frequency shift or competition, for example).

Clearly, bifurcation analysis of the composite-cavity mode model is more complicated than of the coupled-laser model, owing to the implicit dependence of (5.4)–(5.5) on the bifurcation parameters $d$ and $\Delta w$. In fact, one needs to set up a continuation problem where solutions to (5.4)–(5.5) are continued simultaneously with solutions to (5.1) and modal integrals (5.6).

**5.1. Passive composite-cavity modes.** For our system of three coupled lasers with $w_A = w_C$, it follows from (5.1) that the $x$ component of the composite-cavity mode $X_j(x)$ is either symmetric,

$$X_j(x) = X_j(-x), \tag{5.7}$$

Copyright © by SIAM. Unauthorized reproduction of this article is prohibited.

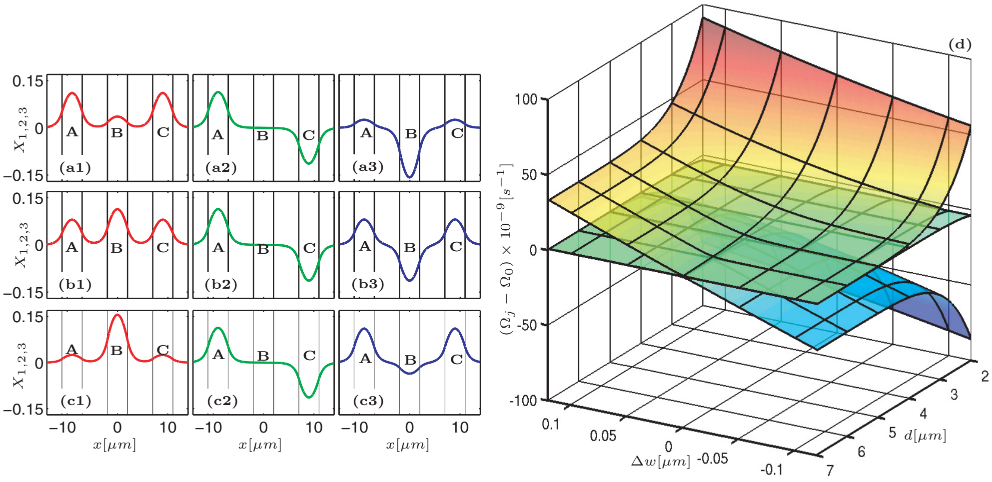

**Figure 18.** *Left:* $X_1(x)$ *(red),* $X_2(x)$ *(green), and* $X_3(x)$ *(blue) calculated for* $d = 5\mu m$ *and* $\Delta w = 0.05\mu m$ (a), $\Delta w = 0\mu m$ (b), *and* $\Delta w = -0.05\mu m$ (c). *Right: The mode frequencies* $\Omega_1$, $\Omega_2$, *and* $\Omega_3$ *(from bottom to top) as a function of the laser distance,* $d$, *and the laser width difference,* $\Delta w$. $\Omega_0$ *is the frequency of a single uncoupled laser.*

or antisymmetric,

$$X_j(x) = -X_j(-x). \tag{5.8}$$

Henceforth, we study nonlinear interactions of three composite-cavity modes: two with a symmetric $x$ component, namely $X_1(x)$ and $X_3(x)$, and one with an antisymmetric $x$ component, namely $X_2(x)$. The three functions $X_j(x)$, where $j = 1, 2$, and 3, are shown in Figure 18 for $\Delta w = -0.05$ $\mu$m, where the two outer lasers are wider than the middle laser ((a1)–(a3)), $\Delta w = 0$ $\mu$m, where all lasers are identical ((b1)–(b3)), and $\Delta w = 0.05$ $\mu$m, where the middle laser is wider than the two outer lasers ((c1)–(c3)). Figure 18(d) shows the nonlinear dependence of the composite-cavity mode frequencies, $\Omega_j$, on the laser distance, $d$, and the width difference, $\Delta w$. For small $d$, the frequency separation between different composite-cavity modes is large and weakly dependent on $\Delta w$. As $d$ decreases, the separation becomes smaller. Specifically, for $\Delta w > 0$ composite-cavity modes 1 and 2 have a similar frequency, whereas for $\Delta w < 0$ composite-cavity modes 2 and 3 have a similar frequency. Changes in $\Delta w$ have a much stronger effect on the frequency of composite modes 1 and 3 than on the frequency of composite mode 2. This is because composite mode 2 has vanishing amplitude in the middle laser for all $\Delta w$.

The spatial symmetries specified by (5.7) and (5.8) impose the following relations between $K^s_{jj'}$:

$$\begin{gathered} K^B_{12} = K^B_{23} = 0, \\ K^A_{11} = K^C_{11}, \qquad K^A_{22} = K^C_{22}, \qquad K^A_{33} = K^C_{33}, \\ K^A_{12} = -K^C_{12}, \qquad K^A_{23} = -K^C_{23}, \qquad K^A_{13} = K^C_{13}, \end{gathered} \tag{5.9}$$

which lead to just 11 (10 nonzero and one zero) independent modal integrals. For small laser distance, $d$, $K^s_{jj'}$ have a weak dependence on $\Delta w$. However, $K^s_{jj'}$ become strongly nonlinear

Copyright © by SIAM. Unauthorized reproduction of this article is prohibited.

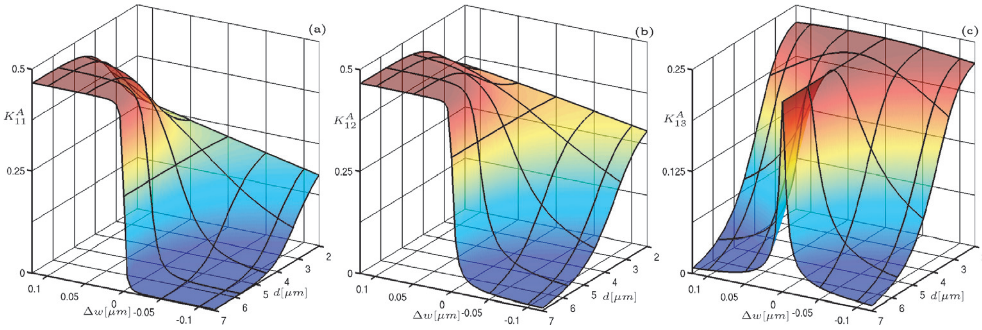

**Figure 19.** *Modal integrals* (a) $K_{11}^A$*,* (b) $K_{12}^A$*, and* (c) $K_{13}^A$ *as a function of the laser distance, $d$, and the laser width difference, $\Delta w$.*

functions of $\Delta w$ at large $d$. Figure 19 illustrates this behavior with the three integrals for composite-cavity mode 1 in laser $A$. In particular, $K_{11}^A$ large for $\Delta w > 0$, and vanishing for $\Delta w < 0$ indicates that mode one is localized in lasers $A$ and $C$ for $\Delta w > 0$ (Figure 19(a)). The integral $K_{22}^A$ is almost constant and $K_{33}^A$ and $K_{11}^B$ are similar to $K_{11}^A$ when $\Delta w$ is replaced with $-\Delta w$ (not shown). Also, $K_{33}^B$ is similar to $K_{11}^A$, and $K_{22}^B$ remains close to zero (not shown). The integral $K_{12}^A$ indicates an abrupt transition from strong to weak spatial coupling between modes 1 and 2 as $\Delta w$ decreases through zero (Figure 19(b)). Similar behavior is found for $K_{23}^A$ when $\Delta w$ is replaced with $-\Delta w$ (not shown). A strong spatial coupling between modes 1 and 3 in lasers $A$ and $C$ for $\Delta w \approx 0$ decays rapidly to zero as $|\Delta w|$ increases (Figure 19(c)). Finally, $K_{13}^A$ is similar to $-K_{13}^B$.

**5.2. Symmetry properties.** Similarly to the coupled-laser model, the composite-cavity mode model (5.1)–(5.5) has $\mathbb{S}^1 \times \mathbb{Z}_2$ symmetry.

The (continuous) $\mathbb{S}^1$ symmetry is due to the equivariance of the vector field defined by (5.4)–(5.5) under the transformation

$$\begin{aligned} T_{\mathbb{S}^1} :&(E_1, E_2, E_3, N_A, N_B, N_C)^T \\ &\longrightarrow (e^{ia}E_1, e^{ia}E_2, e^{ia}E_2, N_A, N_B, N_C)^T \qquad \forall a \in [0, 2\pi). \end{aligned} \tag{5.10}$$

This transformation corresponds to the same phase shift in the fields of all the composite-cavity modes, $E_j$. To facilitate numerical bifurcation analysis, we need to carry out a group orbit reduction. However, we cannot use the same reduction approach as in section 4.1 for the coupled-laser model. This is because the composite-mode amplitudes, $E_j(t)$, vanish on open sets of parameters, where algebraic singularities in the equations for the phase differences prevent numerical bifurcation analysis. An alternative way to reduce $\mathbb{S}^1$ symmetry is to introduce new coordinates, namely $Z_{11}, Z_{22}, Z_{33}, Z_{12}, Z_{13}$, and $Z_{23}$, which are defined by

$$Z_{jj'} = E_j\overline{E}_{j'}, \tag{5.11}$$

and form a set of $\mathbb{S}^1$-invariant monomials [29, 13] (where the bar denotes complex conjugation). This allows periodic $\mathbb{S}^1$ group orbits of (5.4)–(5.5) to be studied as isolated equilibria of the the reduced system that is obtained by replacing the $dE_j/dt$ equations with

$$\frac{dZ_{jj'}}{dt} = \frac{dE_j}{dt}\overline{E}_{j'} + E_j\frac{d\overline{E}_{j'}}{dt} \tag{5.12}$$

Copyright © by SIAM. Unauthorized reproduction of this article is prohibited.

and replacing $E_j\overline{E}_{j'}$ with $Z_{jj'}$ in (5.5). Such a reduced system does not have any algebraic singularities and greatly facilitates numerical continuation. However, one drawback of this approach is that the monomials (5.11) are not all independent and the reduced system is of higher dimension than the original system. This gives rise to additional eigenvalues and the possibility of "bogus" bifurcations, not present in the original system, when these additional eigenvalues cross through zero.

The (discrete) $\mathbb{Z}_2$ symmetry is due to the equivariance of the vector field defined by (5.4)–(5.5) under the linear transformation

$$T_{\mathbb{Z}_2} : (E_1, E_2, E_3, N_A, N_B, N_C)^T \longrightarrow (E_1, -E_2, E_3, N_C, N_B, N_A)^T, \tag{5.13}$$

which corresponds to swapping the two outer lasers. (This equivariance is made more transparent by substituting relations (5.9) into (5.4)–(5.5).)

In the composite-cavity mode model, the representation of the $\mathbb{Z}_2$ symmetry is given by the identity matrix $I_9$ and

$$R_{\mathbb{Z}_2} = \begin{pmatrix} 1 & 0 & 0 & 0 \\ 0 & -1 & 0 & 0 \\ 0 & 0 & 1 & 0 \\ 0 & 0 & 0 & A_3 \end{pmatrix}, \tag{5.14}$$

where $A_3$ is the $3\times 3$ antidiagonal matrix. The fixed-point subspace due to the $\mathbb{Z}_2$ symmetry,

$$\mathrm{Fix}(\mathbb{Z}_2) = \{(E_1, E_2, E_3, N_A, N_B, N_C)^T \in \mathbb{R}^9 : \quad E_2 = 0, \quad N_A = N_C\}, \tag{5.15}$$

is a six-dimensional manifold that is invariant under the transformation (5.13) and under the flow given by (5.4)–(5.5). Given that $U_2(\mathbf{r}) \neq 0$ in lasers $A$ and $C$, it follows that lasers $A$ and $C$ have identical electric fields if and only if $E_2 = 0$. Hence, (5.15) is equivalent to (4.11). As in section 4.1 for the coupled laser model, we can distinguish between *fixed solutions* that lie within the fixed-point subspace $\mathrm{Fix}(\mathbb{Z}_2)$ and *conjugate solutions* that are not in the fixed-point subspace. Specifically, fixed solutions for the composite-cavity mode model have $E_2(t) = 0$, meaning that there are only contributions from the two symmetric composite modes 1 and 3, and the electric fields in the outer lasers are identical. For conjugate solutions, the antisymmetric composite mode has a nonzero amplitude, $E_2(t) \neq 0$, and the electric fields in the outer lasers are different.

**5.3. Phase locking.** In the composite-cavity model, locking all three lasers to the same optical frequency can be represented by two solution types. One type is a single composite-cavity mode solution. Another type is a multi-composite-cavity mode solution where all the modes with nonzero amplitudes are phase locked to a common frequency $\omega^0$ with a possible constant phase shift $\varphi_j^0$:

$$\begin{aligned} E_j(t) &= |E_j^0| e^{-i(\omega^0 t + \varphi_j^0)} \quad \text{for } j = 1,2,3, \\ N_s(t) &= N_s^0 \quad \text{for } s = A, B, C. \end{aligned} \tag{5.16}$$

In the bifurcation and Lyapunov diagrams, the locking regions are shaded in green.

Copyright © by SIAM. Unauthorized reproduction of this article is prohibited.

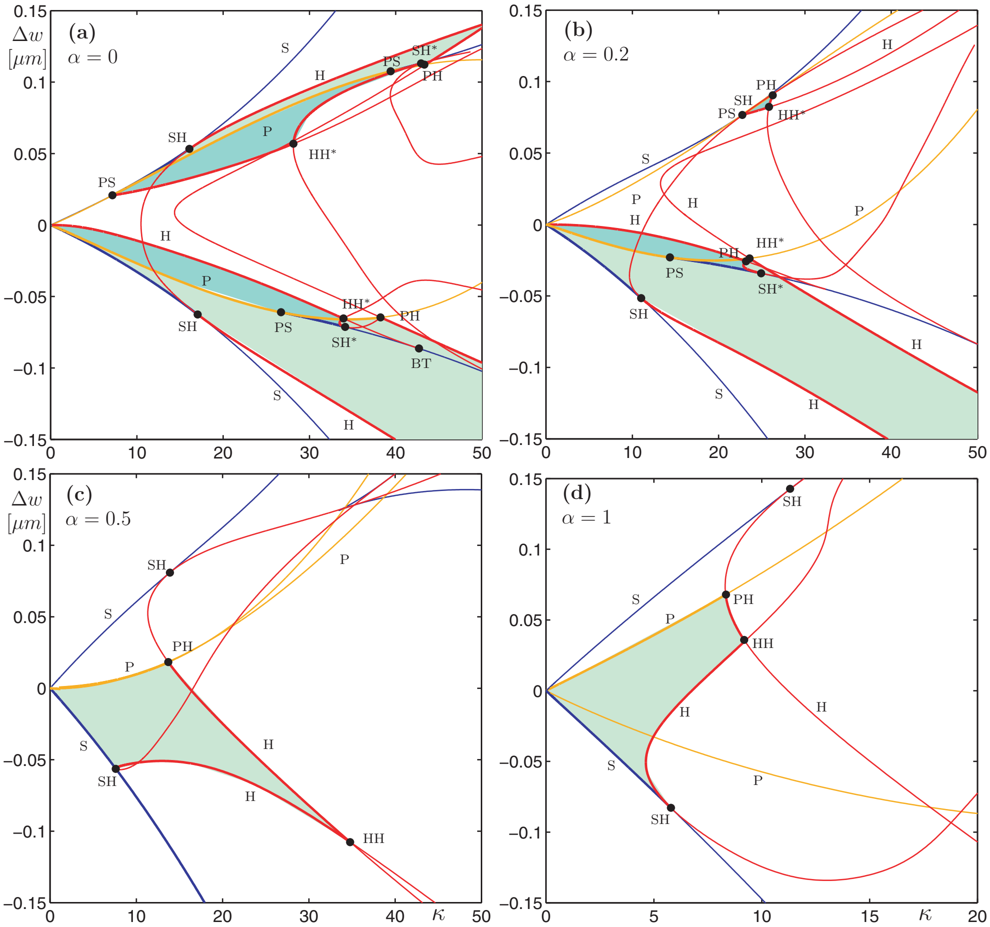

**Figure 20.** *Two-parameter bifurcation diagrams in the* $(\kappa, \Delta w)$ *plane. Regions of locking are shaded in green. Light and dark shading correspond to fixed and conjugate locking* (5.16)*, respectively. From* (a)–(d) $\alpha = 0, 0.2$*,* $0.5$*, and* $1$*. Compare with Figures* 3–4 *for the coupled-laser model* (4.2) *and* (4.8)*. For the labeling and color coding see Table* 3*.*

**5.4. Dynamics of the composite-cavity mode model.** Figure 20 shows the bifurcation diagrams and the locking regions in the $(\kappa, \Delta w)$ plane for four different values of the $\alpha$-parameter. To facilitate a comparison with the coupled-laser model from section 4, we introduce the normalized coupling strength

$$\kappa = Ce^{-p_G d},$$

where the coupling rate $C = 420$ and the inverse coupling length $p_G = 0.98\mu\text{m}^{-1}$ were calculated in [23] for weakly coupled lasers. The laser width difference, $\Delta w$, is related to the frequency detuning, $\Delta$, between the middle and two outer lasers.

For $\alpha = 0$ there are two locking bands off the line $\Delta w = 0$ (Figure 20(a)). Inside the fixed-locking region (light green), the antisymmetric composite-cavity mode has zero amplitude, $|E_2(t)| = 0$, and composite modes 1 and 3 are phase locked to a single frequency. Such a two-composite-mode locking means that the outer lasers $A$ and $C$ have identical electric fields.

Copyright © by SIAM. Unauthorized reproduction of this article is prohibited.

When crossing the pitchfork bifurcations (P) from a light green to a dark green region, an additional solution with $|E_2(t)| > 0$ bifurcates off the fixed-point subspace defined by (5.15). In other words, the antisymmetric composite-cavity mode 2 moves from below to above its lasing threshold. Hence, in the conjugate locking regions (dark green), none of the phase-locked lasers oscillates in phase with another laser.

As the $\alpha$-parameter is increased, the locking regions undergo a number of qualitative and quantitative changes. Specifically, the locking region at $\Delta w > 0$ disappears (Figure 20(b)) at around $\alpha = 0.2$. The locking region at $\Delta w < 0$ becomes bounded towards increasing $\kappa$, and its conjugate component disappears before $\alpha$ reaches 0.5 (Figure 20(c)). For $\alpha > 0.5$, there is only a single (fixed) locking region bounded by a saddle-node curve, two Hopf curves, and a pitchfork curve. This locking region shifts towards $\Delta w = 0$ and expands along the $\Delta w$ direction with increasing $\alpha$ (Figure 20(d)).

On the level of bifurcations of (relative) equilibria, the simpler coupled-laser model shows impressive qualitative and good quantitative agreement with the composite-cavity model, provided that the analysis is restricted to weak coupling between lasers and that the appropriate normalization of the coupling strength is known. The locking regions of both models have very similar structures, are bounded by the same bifurcation types, and have codimension-two points occurring for similar values of $\kappa$. Nonetheless, the agreement is not as “perfect” as for the two-laser system studied in [23]. We note that the bifurcation diagram in Figure 20(a) for $\alpha = 0$ does not have a reflectional symmetry about $\Delta w = 0$. In particular, the upper locking band does not emerge from the origin and the lower locking band is noticeably larger. At any value of the $\alpha$-parameter, the lower locking band remains relatively larger and extends to higher values of $\kappa$ than in the simpler coupled-laser model.

The results obtained from the composite-cavity mode model depend on whether the total width of the system remains constant. Here, the total width of the system varies with $\Delta w$ and (5.4)–(5.5) do not have the parameter symmetry under the transformation $\Delta w \to -\Delta w$. In particular, there is stronger mode amplification owing to larger total laser volume for negative $\Delta w$. The coupled-laser model neglects these spatial effects, which results in the parameter symmetry (4.16).

A comparison between Figure 21 and Figure 10(c) shows that the agreement between the two models holds as well for the global bifurcations described in section 4.5 and for complicated solutions outside the locking region. Specifically, the upper locking boundary in the Lyapunov diagram in Figure 21 coincides with the curve of heteroclinic bifurcations (het) that extends between the origin and the codimension-two Shilnikov–Hopf bifurcation point (ShH*). This heteroclinic bifurcation gives rise to a region of multistability with locked and unlocked dynamics coexisting between het and the upper pitchfork bifurcation curve (P). Towards decreasing $\Delta w$, the locking region is bounded by the saddle-node homoclinic bifurcation (Shom) that meets the homoclinic bifurcation (hom) at the codimension-two noncentral saddle-node homoclinic point (NC). Furthermore, there is a great similarity on the level of quasi-periodic and chaotic dynamics including the intricate structure in the Lyapunov diagram associated with bifurcation cascades accumulating onto hom and het.

**6. Conclusions.** We studied nonlinear dynamics of three linearly coupled laser oscillators using $\mathbb{S}^1$ symmetry reduction, complementary methods for stability analysis, multiparameter

Copyright © by SIAM. Unauthorized reproduction of this article is prohibited.

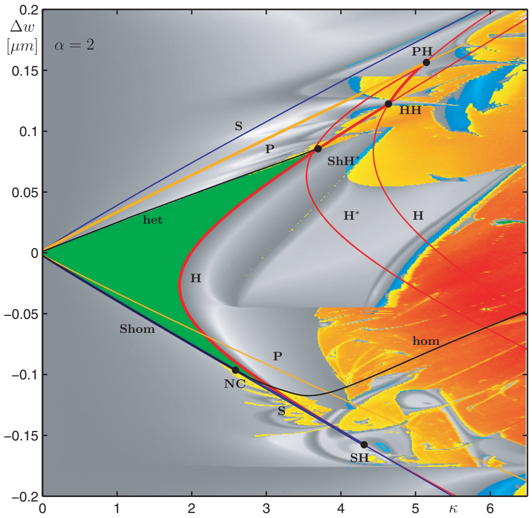

**Figure 21.** *Superposition of the Lyapunov diagram and bifurcation diagram for the composite-cavity mode model* (5.4)–(5.5) *with* $\alpha = 2$*. Compare with Figure* 10(c) *for the coupled-laser model* (4.2) *and* (4.8).

study, and different modeling approaches. The three-laser system is the first step towards the understanding of nonlinear behavior in larger arrays, for which preliminary studies show that many general features of the three-laser system persist.

In a three-parameter study of the *coupled-laser model*, Lyapunov and bifurcation diagrams in the plane of the laser-coupling strength, $\kappa$, and frequency detuning, $\Delta$, were calculated for different but fixed values of the third parameter, $\alpha$, that quantifies coupling between the amplitude and phase of an individual laser. In this way, we uncovered two striking results with increasing $\alpha$: severe changes to the shape and extent of the locking regions (where all three lasers oscillate at the same frequency), and emergence of vast regions of chaos. On the one hand, bifurcation analysis explained the intricate and changing shape of phase locking regions in terms of codimension-two and -three bifurcations. The analysis also highlighted the importance of global homoclinic and heteroclinic bifurcations associated with multistability and complicated locking-unlocking transitions. On the other hand, the $\alpha$-induced stretch-and-fold action creating horseshoes in the laser phase space gave an intuitive explanation for the appearance of vast regions of chaos. The emerging complicated web of codimension-one bifurcations and their infinite cascades linked together via bifurcations of higher codimension, often called *organizing centers*, provided the *backbone* of the coupled-laser dynamics.

The *coupled-laser model* was then compared with a conceptually different but more accurate *composite-cavity model*. Such a comparison was motivated by a need to further understand whether the simpler *coupled-laser model* captures accurately the essential (optical) nonlinearities of laser arrays. We found very good agreement on the level of the locking regions, local and global bifurcations, and chaotic dynamics. Our results support the "simple" coupled-laser approach to modeling arrays of weakly coupled lasers. They also show that understanding large semiconductor laser systems will require (bifurcation) analysis of chaotic attractors that occupy much of the parameter space.

Copyright © by SIAM. Unauthorized reproduction of this article is prohibited.

## REFERENCES

[1] H. Adachihara, O. Hess, R. Indik, and J. V. Moloney, *Semiconductor laser array dynamics: Numerical simulations on multistripe index-guided lasers*, J. Opt. Soc. Amer. B Opt. Phys., 10 (1993), pp. 496–506.

[2] F. T. Arecchi, R. Meucci, and W. Gadomski, *Laser dynamics with competing instabilities*, Phys. Rev. Lett., 58 (1987), pp. 2205–2208.

[3] A. Argyris, D. Syvridis, L. Larger, V. Annovazzi-Lodi, P. Colet, I. Fischer, J. Garcia-Ojalvo, C. R. Mirasso, L. Pesquera, and K. A. Shore, *Chaos-based communications at high bit rates using commercial fibre-optic links*, Nature, 438 (2005), pp. 343–346.

[4] A. Arneodo, P. H. Coullet, E. A. Spiegel, and C. Tresser, *Asymptotic chaos*, Phys. D, 14 (1985), pp. 327–347.

[5] D. G. Aronson, G. B. Ermentrout, and N. Kopell, *Amplitude response of coupled oscillators*, Phys. D, 41 (1990), pp. 403–449.

[6] L. A. Belyakov, *Bifurcation of systems with a homoclinic curve of a saddle-focus with a saddle quantity zero*, Mat. Zametki., 36 (1984), pp. 681–689.

[7] G. Benettin, L. Galgani, A. Giorgilli, and J.-M. Strelcyn, *Lyapunov characteristic exponents for smooth dynamical systems and for Hamiltonian systems; a method for computing all of them. Part* 2*: Numerical application*, Meccanica, 15 (1980), pp. 21–30.

[8] C. Bonatto and J. A. C. Gallas, *Accumulation horizons and period adding in optically injected semiconductor lasers*, Phys. Rev. E, 75 (2007), 055204.

[9] D. Botez and D. R. Scifres, *Diode Laser Arrays*, Cambridge University Press, Cambridge, UK, 1994.

[10] Y. Braiman, T. A. B. Kennedy, K. Wiesenfeld, and A. Khibnik, *Entrainment of solid-state laser arrays*, Phys. Rev. A, 52 (1995), pp. 1500–1506.

[11] A. R. Champneys and A. J. Rodríguez-Luis, *The non-transverse Shil'nikov-Hopf bifurcation: Uncoupling of homoclinic orbits and homoclinic tangencies*, Phys. D, 128 (1999), pp. 130–158.

[12] K. E. Chlouverakis and M. J. Adams, *Stability maps of injection-locked laser diodes using the largest Lyapunov exponent*, Opt. Commun., 216 (2003), pp. 405–412.

[13] P. Chossat, *The reduction of equivariant dynamics to the orbit space for compact group actions*, Acta Appl. Math., 70 (2002), pp. 71–94.

[14] S. N. Chow and X.-B. Lin, *Bifurcation of a homoclinic orbit with a saddle-node equilibrium*, Differential Integral Equations, 3 (1990), pp. 435–466.

[15] W. W. Chow, *A composite-resonator mode description of coupled lasers*, IEEE J. Quantum Electron., 22 (1986), pp. 1174–1183.

[16] W. W. Chow, *Frequency locking in an index-guided semiconductor laser array*, J. Opt. Soc. Amer. B Opt. Phys., 3 (1986), pp. 833–836.

[17] W. W. Chow, S. W. Koch, and M. Sargent III, *Semiconductor Laser Physics*, Springer-Verlag, Berlin, 1997.

[18] W. W. Chow and S. Wieczorek, *Using chaos for remote sensing of laser radiation*, Opt. Express, 17 (2009), pp. 7491–7504.

[19] R. Ciegis, M. Radziunas, and M. Lichtner, *Numerical algorithms for simulation of multisection lasers by using traveling wave model*, Math. Model. Anal., 13 (2008), pp. 327–348.

[20] B. Deng, *Homoclinic bifurcations with nonhyperbolic equilibria*, SIAM J. Math. Anal., 21 (1990), pp. 693–720.

[21] E. J. Doedel, A. R. Champneys, T. F. Fairgieve, Y. A. Kuznetsov, B. Oldeman, R. Paffenroth, B. Sandstede, X. Wang, and C. Zhang, *Auto*-07*p: Continuation and Bifurcation Software for Ordinary Differential Equations*, Technical report, Concordia University, Montreal, Canada, 2007; available online at http://sourceforge.net/projects/auto-07p/.

[22] H. Erzgräber, B. Krauskopf, and D. Lenstra, *Bifurcation analysis of a semiconductor laser with filtered optical feedback*, SIAM J. Appl. Dyn. Syst., 6 (2007), pp. 1–28.

[23] H. Erzgräber, S. Wieczorek, and B. Krauskopf, *Dynamics of two laterally coupled semiconductor lasers: Strong- and weak-coupling theory*, Phys. Rev. E, 78 (2008), 066201.

[24] H. Erzgräber, S. Wieczorek, and B. Krauskopf, *Locking behavior of three coupled laser oscillators*, Phys. Rev. E, 80 (2009), 026212.

Copyright © by SIAM. Unauthorized reproduction of this article is prohibited.

[25] H. Erzgräber, S. Wieczorek, and B. Krauskopf, *Dynamics of two semiconductor lasers coupled by a passive resonator*, Phys. Rev. E, 81 (2010), 056201.

[26] L. Fabiny, P. Colet, R. Roy, and D. Lenstra, *Coherence and phase dynamics of spatially coupled solid-state lasers*, Phys. Rev. A, 47 (1993), pp. 4287–4296.

[27] W. Fader, *Theory of two coupled lasers*, IEEE J. Quantum Electron., 21 (1985), pp. 1838–1844.

[28] M. Golubitsky and I. Stewart, *The Symmetry Perspective—From Equilibrium to Chaos in Phase Space and Physical Space*, Birkhäuser Verlag, Basel, 2002.

[29] M. Golubitsky, I. Stewart, and D. G. Schaeffer, *Singularities and Groups in Bifurcation Theory: Volume* II, Springer-Verlag, New York, 1985.

[30] J. Guckenheimer and P. Holmes, *Nonlinear Oscillations, Dynamical Systems, and Bifurcations of Vector Fields*, Springer-Verlag, New York, 1983.

[31] H. Haken, *Laser Theory*, Springer-Verlag, Heidelberg, 1970.

[32] T. Heil, I. Fischer, W. Elsässer, J. Mulet, and C. R. Mirasso, *Chaos synchronization and spontaneous symmetry-breaking in symmetrically delay-coupled semiconductor lasers*, Phys. Rev. Lett., 86 (2001), pp. 795–798.

[33] C. H. Henry, *Theory of the linewidth of semiconductor lasers*, IEEE J. Quantum Electron., 18 (1982), pp. 259–264.

[34] O. Hess and E. Schöll, *Spatio-temporal dynamics in twin-stripe semiconductor lasers*, Phys. D, 70 (1994), pp. 165–177.

[35] P. Hirschberg and E. Knobloch, *Sil'nikov-Hopf bifurcation*, Phys. D, 62 (1993), pp. 202–216.

[36] A. Hohl, A. Gavrielides, T. Erneux, and V. Kovanis, *Localized synchronization in two coupled nonidentical semiconductor lasers*, Phys. Rev. Lett., 78 (1997), pp. 4745–4748.

[37] A. Jechow, M. Lichtner, R. Menzel, M. Radziunas, D. Skoczowsky, and A. G. Vladimirov, *Stripe-array diode-laser in an off-axis external cavity: Theory and experiment*, Opt. Express, 17 (2009), pp. 19599–19604.

[38] E. Kapon, J. Katz, and A. Yariv, *Supermode analysis of phase-locked arrays of semiconductor lasers*, Opt. Lett., 9 (1984), pp. 125–127.

[39] G. Kozyreff, A. G. Vladimirov, and P. Mandel, *Dynamics of a semiconductor laser array with delayed global coupling*, Phys. Rev. E, 64 (2001), 016613.

[40] B. Krauskopf and D. Lenstra, eds., *Fundamental Issues of Nonlinear Laser Dynamics*, American Institute of Physics, Melville, NY, 2000.

[41] B. Krauskopf and S. Wieczorek, *Accumulating regions of winding periodic orbits in optically driven lasers*, Phys. D, 173 (2002), pp. 97–113.

[42] Y. A. Kuznetsov, *Elements of Applied Bifurcation Theory*, Springer-Verlag, New York, 2004.

[43] R.-D. Li and T. Erneux, *Stability conditions for coupled lasers: Series coupling versus parallel coupling*, Opt. Commun., 99 (1993), pp. 196–200.

[44] R.-D. Li and T. Erneux, *Bifurcation to standing and traveling waves in large arrays of coupled lasers*, Phys. Rev. A, 49 (1994), pp. 1301–1312.

[45] F.-Y. Lin and J.-M. Liu, *Chaotic radar using nonlinear laser dynamics*, IEEE J. Quantum Electron., 40 (2004), pp. 815–820.

[46] K. K. Lin and L.-S. Young, *Shear-induced chaos*, Nonlinearity, 21 (2008), pp. 899–922.

[47] A. M. Lindberg, T. Fordell, and S. Valling, *Dynamics, bifurcations and chaos in coupled lasers*, Philos. Trans. R. Soc. Lond. Ser. A Math. Phys. Eng. Sci., 366 (2008), pp. 427–435.

[48] B. Liu, Y. Liu, and Y. Braiman, *Coherent addition of high power laser diode array with a v-shape external talbot cavity*, Opt. Express, 16 (2008), pp. 20935–20942.

[49] P. Mandel, *Theoretical Problems in Cavity Nonlinear Optics*, Cambridge University Press, Cambridge, UK, 2005.

[50] P. Mandel, R.-D Li, and T. Erneux, *Pulsating self-coupled lasers*, Phys. Rev. A, 39 (1989), pp. 2502–2508.

[51] M. Matus, J. V. Moloney, and M. Kolesik, *Relevance of symmetry for the synchronization of chaotic optical systems and the related Lang-Kobayashi model limitations*, Phys. Rev. E, 67 (2003), 016208.

[52] D. Merbach, O. Hess, H. Herzel, and E. Schöll, *Injection-induced bifurcations of transverse spatiotemporal patterns in semiconductor laser arrays*, Phys. Rev. E, 52 (1995), pp. 1571–1578.

Copyright © by SIAM. Unauthorized reproduction of this article is prohibited.

[53] C. R. Mirasso, M. Kolesik, M. Matus, J. K. White, and J. V. Moloney, *Synchronization and multimode dynamics of mutually coupled semiconductor lasers*, Phys. Rev. A, 65 (2001), 013805.

[54] K. Otsuka, *Self-induced phase turbulence and chaotic itinerancy in coupled laser systems*, Phys. Rev. Lett., 65 (1990), pp. 329–332.

[55] E. Ott, *Chaos in Dynamical Systems*, Cambridge University Press, Cambridge, UK, 2002.

[56] J. J. Raftery, Jr., A. J. Danner, J. C. Lee, and K. D. Choquette, *Coherent coupling of two-dimensional arrays of defect cavities in photonic crystal vertical cavity surface-emitting lasers*, Appl. Phys. Lett., 86 (2005), 201104.

[57] S. Riyopoulos, *Coherent phase locking, collective oscillations, and stability in coupled vertical-cavity-surface emitting laser arrays*, Phys. Rev. A, 66 (2002), 053820.

[58] F. Rogister and R. Roy, *Localized excitations in arrays of synchronized laser oscillators*, Phys. Rev. Lett., 98 (2007), 104101.

[59] F. Rogister, K. S. Thornburg, Jr., L. Fabiny, M. Moller, and R. Roy, *Power-law spatial correlations in arrays of locally coupled lasers*, Phys. Rev. Lett., 92 (2004), 093905.

[60] R. Roy, T. W. Murphy, T. D. Maier, Z. Gills, and E. R. Hunt, *Dynamical control of a chaotic laser: Experimental stabilization of a globally coupled system*, Phys. Rev. Lett., 68 (1992), pp. 1259–1262.

[61] R. Roy and K. S. Thornburg, *Experimental synchronization of chaotic lasers*, Phys. Rev. Lett., 72 (1994), pp. 2009–2012.

[62] P. Ru, P. K. Jakobsen, J. V. Moloney, and R. A. Indik, *Generalized coupled-mode model for the multistripe index-guided laser arrays*, J. Opt. Soc. Amer. B Opt. Phys., 10 (1993), pp. 507–515.

[63] M. Sargent III, M. O. Scully, and W. E. Lamb, Jr., *Laser Physics*, Addison–Wesley, New York, 1974.

[64] S. A. Shakir and W. W. Chow, *Semiclassical theory of coupled lasers*, Opt. Lett., 9 (1984), pp. 202–204.

[65] S. A. Shakir and W. W. Chow, *Semiclassical theory of coupled lasers*, Phys. Rev. A, 32 (1985), pp. 983–991.

[66] J. Sieber, *Numerical bifurcation analysis for multisection semiconductor lasers*, SIAM J. Appl. Dyn. Syst., 1 (2002), pp. 248–270.

[67] M. Silber, L. Fabiny, and K. Wiesenfeld, *Stability results for in-phase and splay-phase states of solid-state laser arrays*, J. Opt. Soc. Amer. B Opt. Phys., 10 (1993), pp. 1121–1129.

[68] S. Smale, *Differentiable dynamical systems*, Bull. Amer. Math. Soc., 73 (1967), pp. 747–817.

[69] M. B. Spencer and W. E. Lamb, Jr., *Laser with a transmitting window*, Phys. Rev. A, 5 (1972), pp. 884–892.

[70] M. B. Spencer and W. E. Lamb, Jr., *Theory of two coupled lasers*, Phys. Rev. A, 5 (1972), pp. 893–898.

[71] G. H. M. Van Tartwijk and G. P. Agrawal, *Laser instabilities: A modern perspective*, Prog. Quantum Electron., 22 (1998), pp. 43–122.

[72] J. R. Terry, K. S. Thornburg, D. J DeShazer, G. D. VanWiggeren, S. Zhu, P. Ashwin, and R. Roy, *Synchronization of chaos in an array of three lasers*, Phys. Rev. E, 59 (1999), pp. 4036–4043.

[73] K. S. Thornburg, M. Möller, R. Roy, T. W. Carr, R.-D Li, and T. Erneux, *Chaos and coherence in coupled lasers*, Phys. Rev. E, 55 (1997), pp. 3865–3869.

[74] A. Uchida, K. Amano, M. Inoue, K. Hirano, S. Naito, H. Someya, I. Oowada, T. Kurashige, M. Shiki, S. Yoshimori, K. Yoshimura, and P. Davis, *Fast physical random bit generation with chaotic semiconductor lasers*, Nat. Photon, 2 (2008), pp. 728–732.

[75] Q. Wang and L.-S. Young, *Strange attractors with one direction of instability*, Comm. Math. Phys., 218 (2001), pp. 1–97.

[76] Q. Wang and L.-S. Young, *Strange attractors in periodically-kicked limit cycles and Hopf bifurcations*, Comm. Math. Phys., 40 (2003), pp. 509–529.

[77] C. O. Weiss and R. Vilaseca, *Dynamics of Lasers*, VCH, Weinheim, Germany, 1991.

[78] H. Wenzel, U. Bandelow, H.-J. Wünsche, and J. Rehberg, *Mechanisms of fast self pulsations in two-section DFB lasers*, IEEE J. Quantum Electron., 32 (1996), pp. 69–78.

[79] J. K. White, M. Matus, and J. V. Moloney, *Achronal generalized synchronization in mutually coupled semiconductor lasers*, Phys. Rev. E, 65 (2002), 036229.

[80] S. Wieczorek, *Stochastic bifurcation in noise-driven lasers and Hopf oscillators*, Phys. Rev. E, 79 (2009), 036209.

Copyright © by SIAM. Unauthorized reproduction of this article is prohibited.

[81] S. Wieczorek and W. W. Chow, *Global view of nonlinear dynamics in coupled-cavity lasers—a bifurcation study*, Opt. Commun., 246 (2005), pp. 471–493.

[82] S. Wieczorek, B. Krauskopf, and D. Lenstra, *A unifying view of bifurcations in a semiconductor laser subject to optical injection*, Opt. Commun., 172 (1999), pp. 279–295.

[83] S. Wieczorek, B. Krauskopf, T. B. Simpson, and D. Lenstra, *The dynamical complexity of optically injected semiconductor lasers*, Phys. Rep., 416 (2005), pp. 1–128.

[84] S. Wiggins, *Global Bifurcations and Chaos: Analytical Methods*, Springer-Verlag, New York, 1988.

[85] H. G. Winful and L. Rahman, *Synchronized chaos and spatiotemporal chaos in arrays of coupled lasers*, Phys. Rev. Lett., 65 (1990), pp. 1575–1578.

[86] H.-J. Wünsche, S. Bauer, J. Kreissl, O. Ushakov, N. Korneyev, F. Henneberger, E. Wille, H. Erzgräber, M. Peil, W. Elsässer, and I. Fischer, *Synchronization of delay-coupled oscillators: A study of semiconductor lasers*, Phys. Rev. Lett., 94 (2005), 163901.

[87] S. Yanchuk, K. R. Schneider, and L. Recke, *Dynamics of two mutually coupled semiconductor lasers: Instantaneous coupling limit*, Phys. Rev. E, 69 (2004), 056221.

Copyright © by SIAM. Unauthorized reproduction of this article is prohibited.